Quarterly Report for

Contract DE-FG07-02ID14418

Stanford Geothermal Program

January-March 2003

Table of Contents

1. STEAM-WATER RELATIVE PERMEABILITY IN FRACTURES

This project is being conducted by Research Assistant Chih-Ying Chen, Senior Research Engineer Kewen Li and Prof. Roland Horne. The goal of this research has been to gain better understanding of steam-water transport through fractured media and determine the behavior of relative permeability in fractures. From the preliminary results of the unsteady experiment in this research, steam-water flow in fractures shows a different behavior from nitrogen-water flow. The average steam-water relative permeabilities show less phase interference, and behave closer to the X-curve. To confirm this result and obtain more accurate and consistent steam-water relative permeabilities, steady-state experiments are conducted. Amongst them, steady-state nitrogen-water experiments are finished and discussed in this report. The steady-state steam-water experiment is in progress.

1.1 THEORETICAL BACKGROUND

Multiphase flow is an important mechanism in geothermal reservoirs, which are complex systems of porous and fractured media. Complete understanding of geothermal fluid flow requires knowledge of flow in both media. Normally, fractures are the main conduits for fluid. In geothermal reservoirs, the fluids, steam and water, are both derived from the same substance but in different phases. The phase change during steam-water flow is a physical phenomenon that does not occur in the multiphase flow of distinct fluids such as air and water, hence the multiphase flow properties are likely to differ. At present, the governing flow mechanism for boiling multiphase flow in fractures is still undetermined. There are two approaches commonly used to model multiphase flow in fractures, the porous medium approach and the equivalent homogeneous single-phase approach.

The porous medium approach treats fractures as connected two-dimensional porous media. In this model, a pore space occupied by one phase is not available for flow for the other phase. A phase can move from one position to another only upon establishing a continuous flow path for itself. As in porous media, the competition for pore occupancy is described by relative permeability and governed by Darcy's law. Darcy's law for single-phase liquid system is:

$$u_l = \frac{k_{abs}(p_i - p_o)}{\mu_l L} \tag{1.1}$$

where subscript l stands for the liquid phase, i for inlet and o for outlet; μ, p, L, u, k_{abs} are the viscosity, pressure, fracture length, Darcy flow velocity and absolute permeability respectively. The Darcy flow velocity is equal to

$$u = \frac{q}{bw} \tag{1.2}$$

with q as the volumetric flow rate, b the fracture aperture and w as the fracture width. The absolute permeability of a smooth-walled fracture is a function only of the fracture aperture (Witherspoon et al., 1980) as described in the relationship:

$$k_{abs} = \frac{b^2}{12} \tag{1.3}$$

For liquid phase in two-phase flow, Eq. 1.1 becomes

$$u_l = \frac{k_{abs} k_{rl} (p_i - p_o)}{\mu_l L} \tag{1.4}$$

where k_{rl} is the relative permeability of the liquid phase.

Similarly, Darcy's law derived for single-phase isothermal gas flow in porous media (Scheidegger, 1974) is:

$$u_g = \frac{k_{abs} (p_i^2 - p_o^2)}{2\mu_g L p_o} \tag{1.5}$$

with the subscript g pertaining to the gas phase.

In two-phase flow, Eq. 1.5 becomes

$$u_g = \frac{k_{abs} k_{rg} (p_i^2 - p_o^2)}{2\mu_g L p_o} \tag{1.6}$$

with k_{rg} as the gas relative permeability. The sum of the k_{rl} and k_{rg} indicates the extent of phase interference. A sum of relative permeabilities equal to one means the absence of phase interference. Physically this implies that each phase flows in its own path without impeding the flow of the other. The lower is the sum of the relative permeabilities below 1, the greater is the phase interference.

Relative permeability functions are usually taken to be dependent on phase saturation. The two most commonly used expressions for relative permeability for homogeneous porous media are the X-curve and the Corey curve (Corey, 1954). The X-curve defines relative permeability as a linear function of saturation:

$$k_{rl} = S_l \tag{1.7}$$

$$k_{rg} = S_g \tag{1.8}$$

where S_l and S_g are the liquid and gas saturation respectively. The Corey curves relate relative permeability to the irreducible or residual liquid and gas saturation, S_{rl} and S_{rg} :

$$k_{rl} = S^{*4} \tag{1.9}$$

$$k_{rg} = (1 - S^*)^2 (1 - S^{*2}) \tag{1.10}$$

$$S^* = (S_l - S_{rl}) / (1 - S_{rl} - S_{rg}) \tag{1.11}$$

The equivalent homogeneous single-phase approach treats flow through fractures as a limiting case of flow through pipes. In this model, phase velocities in the fracture are equal and capillary forces are negligible. A continuous flow path is not required for movement of each phase. A phase can be carried along by one phase as bubbles, slug or other complex structures. As in pipes, flow can be described by the concept of friction factors and using averaged properties (Fourar et al., 1993):

$$\frac{(p_i - p_o)}{L} = \frac{\Pi f \rho_m V_m^2}{2A} \tag{1.12}$$

where Π is the fracture perimeter, A is the cross sectional area to flow, ρ_m average density and V_m as average flow velocity. The average density is described by:

$$\rho_m = \frac{\rho_g q_g + \rho_l q_l}{q_g + q_l} \tag{1.13}$$

The average flow velocity is equal to:

$$V_m = \frac{q_g + q_l}{A} \tag{1.14}$$

The friction factor, *f*, is derived empirically as a function of the averaged Reynolds number calculated by:

$$N_{\mathrm{Re}} = \frac{2bV_m\rho_m}{\mu_m} \tag{1.15}$$

with μ_m as average viscosity:

$$\mu_m = \frac{\mu_g q_g + \mu_l q_l}{q_g + q_l} \tag{1.16}$$

There are several expressions used to relate friction factor and Reynold's number. The commonly used one for flow through fracture is the generalized Blasius form (Lockhart and Martinelli, 1949):

$$f = \frac{C}{N_{\mathrm{Re}}^n} \tag{1.17}$$

with *C* and *n* as constants derived from experimental data.

According to the results from Diomampo (2001), nitrogen-water flow through fractures is described more appropriately by using the porous medium (relative permeability) approach based on the observations of the multiphase flow behavior. However in the steam-water case, the applicability of the two models for multiphase flow through fractures is still undetermined. From the preliminary results in this research, the steam-water flow shows a different behavior from the nitrogen-water case reported by Diomampo (2001).

1.2 LITERATURE REVIEW

The fluids in geothermal reservoirs, steam and water, are both derived from the same substance. However, they form different phases. The phase change during steam-water multiphase flow has made it difficult to investigate steam-water relative permeability. Even in multiphase flow without boiling, few published data are available for two-phase flow in fractures. Most of the studies have been done for air-water systems or for water-oil systems.

Previous work on multiphase flow in fractures includes Romm's (1966) experiment with kerosene and water through an artificial parallel-plate fracture lined with strips of polyethylene or waxed paper. Romm found a linear relationship between permeability and saturation, $S_w = k_{rw}$, $S_{nw} = k_{rnw}$ such that $k_{rw}+k_{rnw} = 1$ which represents the X-curve behavior. Fourar et al. (1993) artificially roughened glass plates with beads and flowed an air-water mixture between them. Fourar and Bories (1995) did similar experiments using

smooth glass plates and clay bricks. Both studies observed flow structures like bubbles, annular and fingering bubbles comparable to flow in pipes and depicted flow in fractures to be better correlated using the equivalent homogeneous single-phase model. Pan et al. (1996) observed the identical flow structures in their experiments with an oil-water system. They observed that a discontinuous phase can flow as discrete units along with the other phase. Pan et al. (1996) also found their experimental pressure drop to be better predicted by a homogenous single-phase model. All of these experiments showed significant phase interference at intermediate saturations.

Pruess and Tsang (1990) conducted numerical simulation of flow through rough-walled fractures. They modeled fractures as two-dimensional porous media with apertures varying with position. Their study showed the sum of the relative permeabilities to be less than 1, the residual saturation of the nonwetting phase to be large and phase interference to be greatly dependent on the presence or absence of spatial correlation of aperture in the direction of flow. Persoff et al. (1991) did experiments on gas and water flow through rough-walled fractures using transparent casts of natural fractured rocks. The experiment showed strong phase interference similar to the flow in porous media. The relative permeability data of Persoff (1991) and Persoff and Pruess (1995) for flow through rough-walled fractures were compared in Horne et al. (2000) against commonly used relative permeability relations for porous media, the X-curve and Corey curve, as shown in Figure 1.1. Diomampo (2001) performed experiments of nitrogen and water flow through both smooth- and rough-walled artificial fractures, leading to results that are also included in Figure 1.1.

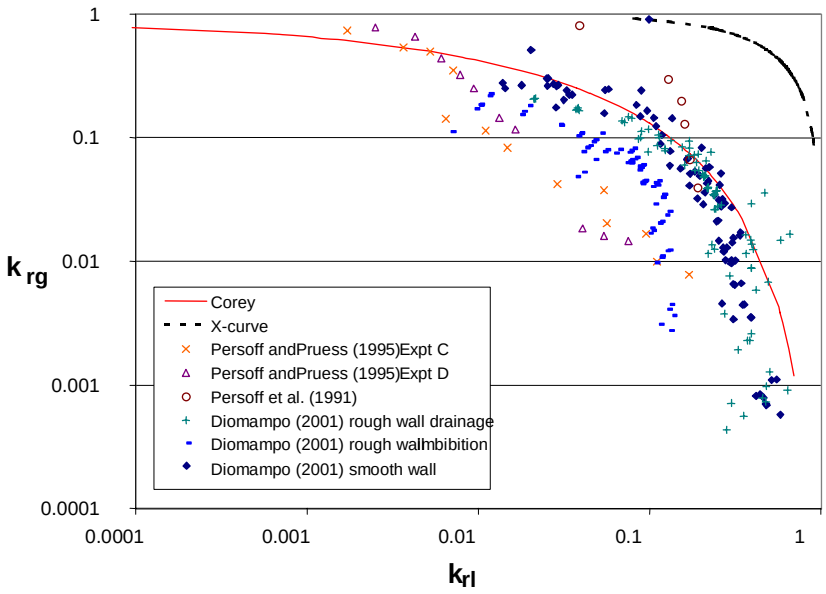

Figure 1.1: Compendium of previous measurements of air-water relative permeabilities in fractures (from Diomampo, 2001).

In the experiments of both Persoff (1991) and Persoff and Pruess (1995), flow of a phase was characterized by having a localized continuous flow path that is undergoing blocking and unblocking by the other phase. Recent parallel plate experiments by Su et al. (1999)

illustrate the same flow mechanism of intermittent localized fluid flow. Kneafsy and Pruess (1998) observed similar intermittent flow in their experiments with pentane through various parallel plate models made from glass, sandblasted glass or transparent fracture replicas. Diomampo (2001) also observed the intermittent phenomenon in her experiments. Furthermore, the results from Diomampo (2001) conform mostly to the Corey type of relative permeability curve (Figure 1.1). This suggests that flow through fractures can be analyzed by treating it as a limiting case of porous media flow and by using the relative permeability approach. These observations are contrary to the findings of Fourar et al (1993), Fourar and Bories (1995), and Pan et al. (1996).

Presently, the flow mechanism and the characteristic behavior of relative permeability in fractures are still not well determined. Issues such as whether a discontinuous phase can travel as discrete units carried along by another phase or will be trapped as residual saturation as in porous medium are unresolved. The question of phase interference i.e. whether the relative permeability curve against saturation is described by an X-curve, Corey or some other function, is still unanswered. The main objective of this study was to contribute to the resolution of these issues. Experiments on flow through smooth-walled and rough-walled fractures without boiling have been conducted by Diomampo (2001), who initially established a methodology for flow characterization and relative permeability calculation for nitrogen-water flow. A more sophisticated and reliable methodology was modified and used for relative permeability experiments in steam- and nitrogen-water flows in this research. Currently, the steady-state, steam-water experiment is in progress.

1.3 EXPERIMENTAL METHODOLOGY

The steam-water flow experiment is more complex than air-water experiment conducted previously by Diomampo (2001). The steam-water flow experiment has to be performed at high temperature, and there is a fundamental difficulty measuring how much of the fluid flows as steam and how much as liquid. The whole experiment system is illustrated in Figure 1.2, which shows the deaerated water supply, the fracture apparatus (inside the air bath), data acquisition system, and digital image recording (also see Figure 1.18).

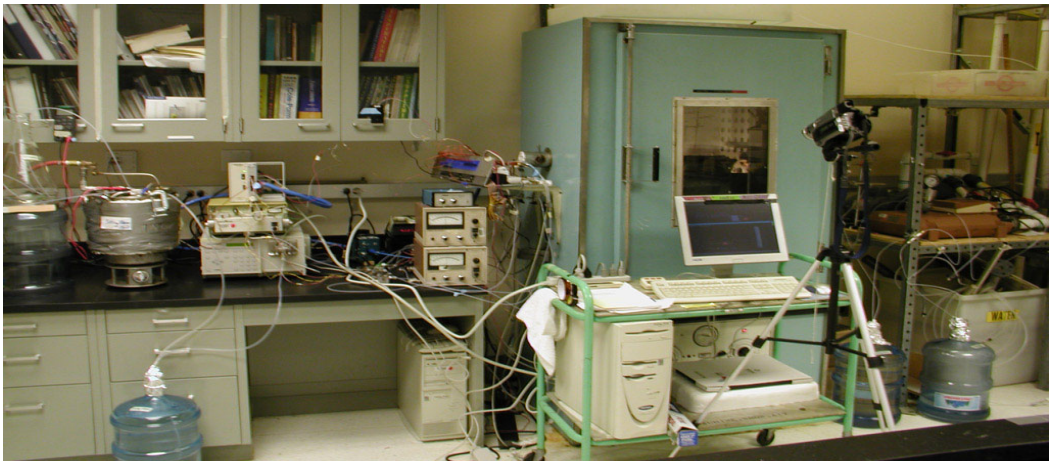

Figure 1.2: Picture of steam-water flow through fracture apparatus.

Fracture Apparatus Description

The fracture is created by a smooth glass plate on top of an aluminum plate, confined by a metal frame bolted to the bottom plate. The frame was designed to improve the seal and to prevent deformation of the glass due to system pressure. The metal frame has several windows and a mirror attached to it for flow visualization (see Figure 1.3 and Figure 1.4.)

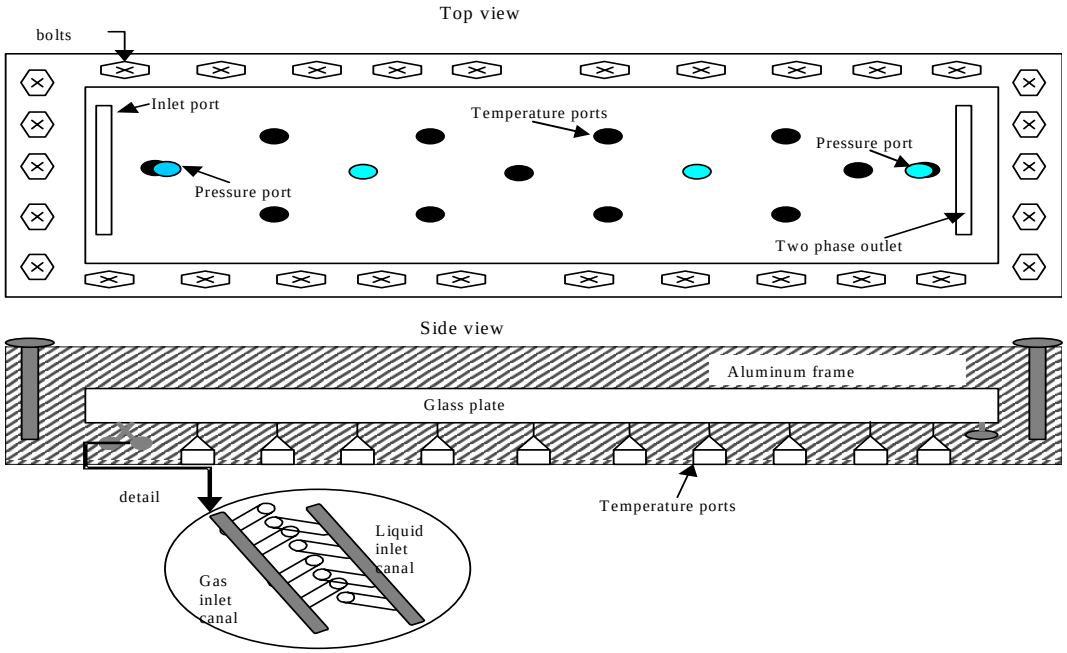

Figure 1.3: Schematic diagram of fracture apparatus.

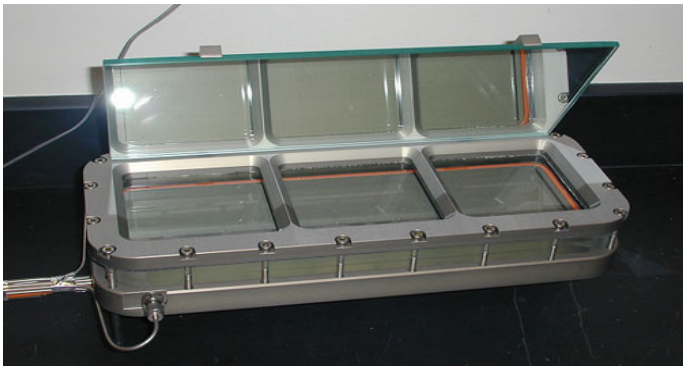

Figure 1.4: Picture of fracture apparatus.

An O-ring (Viton 1/8" thick #2-272) was placed in between the glass and aluminum plate as a seal (see orange color lining in Figure 1.4). Placing this O-ring in the channel was not sufficient to provide a good seal because the channel was custom made in width and length. Thinly cut rubber sheets were placed at the outer boundary to push the O-ring to the sides of the aluminum plate. These provided an excellent seal when compressed with the glass and metal frame. Since the O-ring is cylindrical in shape and the aluminum plate is rectangular, there is a narrow channel in between the O-ring and the plate when squeezed together. A thin lining of copper-based adhesive (Permatex Ultra Copper) was

applied to fill this channel. It is important to eliminate this channel for it serves as an easy conduit for the fluid to pass through instead of the fracture.

The phases enter the fracture through two separate canals. Each canal has several ports drilled in a way that they align on the surface (see Figure 1.3). In the nitrogen-water experiments both entry canals were used, but in the steam-water experiments only water was injected and the steam was created by boiling within the fracture itself. The surface of the fracture apparatus was designed such that there is an available 12 inch by 4 inch space for flow. Throughout this flow area, tiny temperature ports the size of needles were drilled. Needle-size ports were drilled so as to minimize surface discontinuity. A pressure port was drilled at each end of the flow path. The two-phase fluid exits through a single outlet. The apparatus was designed to be of sufficient length that end effects only influence a small part of the flow window – experimental observations have confirmed this to be true.

Pressure Transducers

Low-range differential transducers were used to measure the pressure drop through the fracture, as well as the intermediate pressure and the two-phase outlet pressure. Two liquid differential transducers (Validyne Transducer, model DP-15, range 0-2psi) were attached to four pressure ports inside the fracture to measure the pressure drop through the fracture. Another transducer (Validyne Transducer, model DP-15, range 0-5psi) was attached to the middle point of the fracture. The fourth transducer (Validyne Transducer, model DP-15, range 0-5psi) was attached to the two-phase outlet of the fracture apparatus. These transducers send electrical signals to the SCXI-1000 data acquisition device, which was monitored using the LabView® programmable virtual instrument software. The complete improved measurement configuration in the fracture apparatus is shown in Figure 1.5(a) and (b).

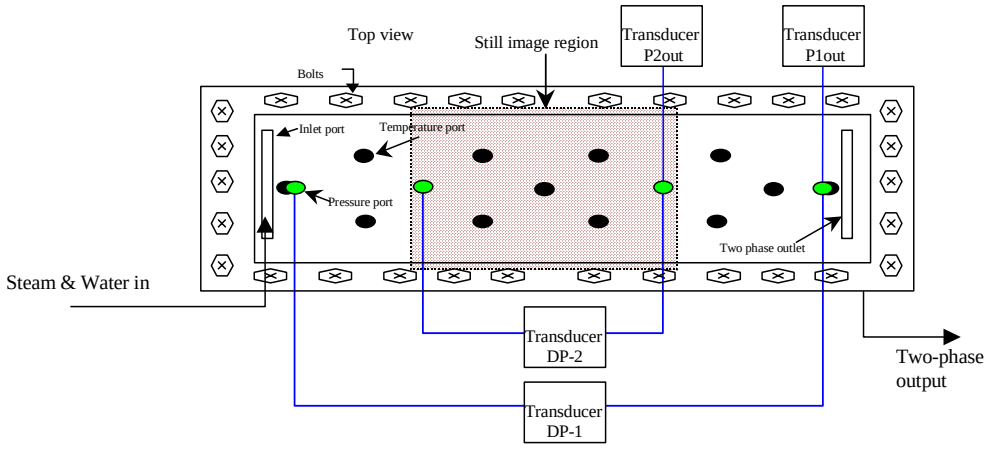

(a) Steam-water steady experiments.

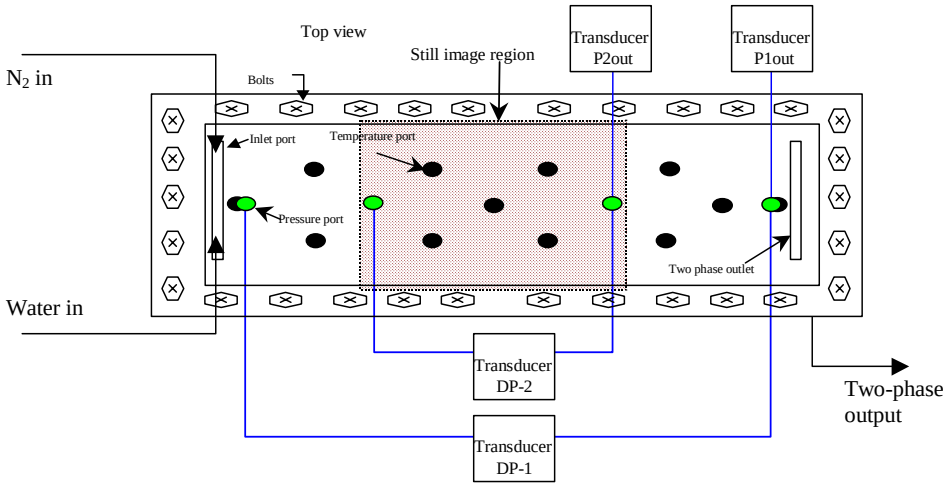

(b) Nitrogen-water steady experiments.

Figure 1.5: Schematic diagrams of pressure measurements in fracture apparatus in steady experiments. (a) Steam-water steady experiments. (b) Nitrogen-water steady experiments.

Capillary end effect was another issue that influenced the previous unsteady experiment. In the current experiments, two new pressure ports were drilled along the fracture for intermediate pressure difference measurement to minimize capillary end effect and to facilitate intermediate absolute pressure measurement through the fracture. Another issue that affects the pressure measurement is the phase transformation inside the pressure tubing. Since experiments were conducted at a temperature nearly boiling point of water, the water-filled pressure tubing connected to the pressure transducers has a tendency to boil. This means both liquid water and gas would coexist inside the pressure tubing. This situation can be illustrated in Figure 1.6. Insensitive and erratic pressure response was obtained due to the different compressibility in water and gas and the solubility of gas. An additional outer cooling tubing was added to cool down the pressure tubing to minimize this two-phase phenomenon inside the pressure tubing. This cooling tubing is expected to quench the pressure tubing and maintain the content inside the pressure tubing in the liquid phase (water). The new plumbing of the pressure measurement is shown in Figure 1.7.

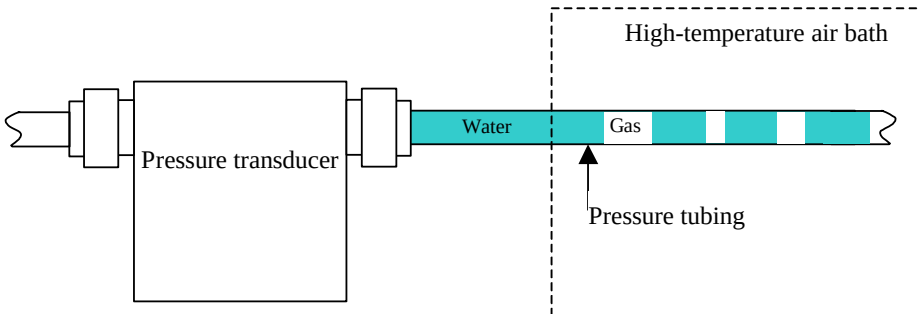

Figure 1.6: Two-phase problem inside the pressure tubing.

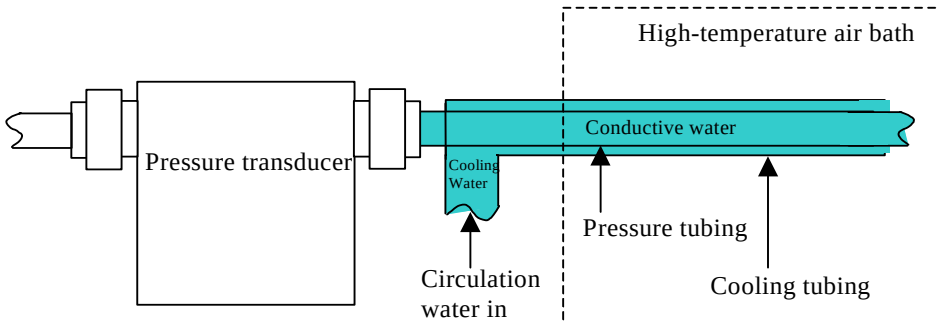

Figure 1.7: Improved plumbing of the pressure measurement to reduce two-phase problem shown in Figure 1.6.

Fractional Flow Ratio Detector (FFRD)

One of the main challenges of the steam-water flow experiment was to measure the steam and water flow rates, since there is phase transition occurring when steam and water flow through the fracture. Therefore using flow meters to measure the rate of each phase becomes inappropriate, because it is always impossible to separate steam from water without any mass loss or gain. To overcome this situation, an in-situ fractional flow ratio detector (FFRD) was designed and constructed as shown in Figure 1.8. The principal of the FFRD is that different phases will have different refractive indices. A phototransistor (NTE 3038, NPN-Si, Visible, Vcbo 25V, Ic 20mA, Pd 50 mW, response time 1.5 μs) was installed inside the FFRD, producing different voltages when sensing different strengths of light. The water phase produces a higher voltage when flowing through the FFRD. In order to minimize the heat loss between the outlet of the fracture apparatus and the FFRD, the FFRD device was installed as close to the outlet of the fracture as possible (about 5cm distance). An example of the FFRD response signal during testing is shown in Figure 1.9.

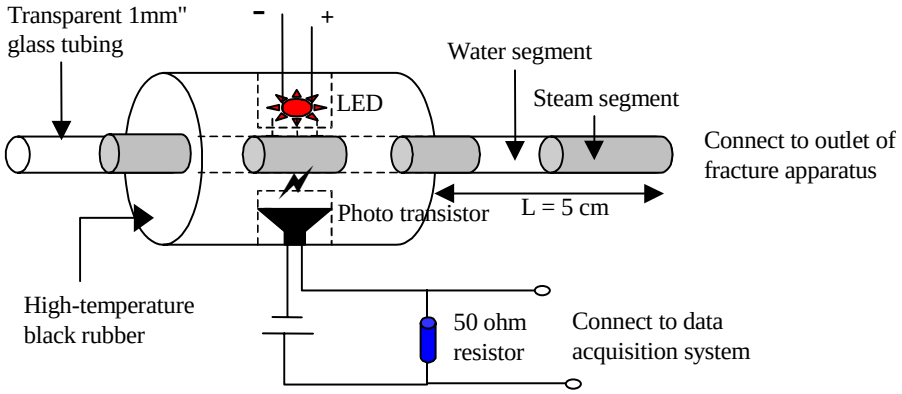

Figure 1.8: Schematic of fractional flow ratio detector (FFRD).

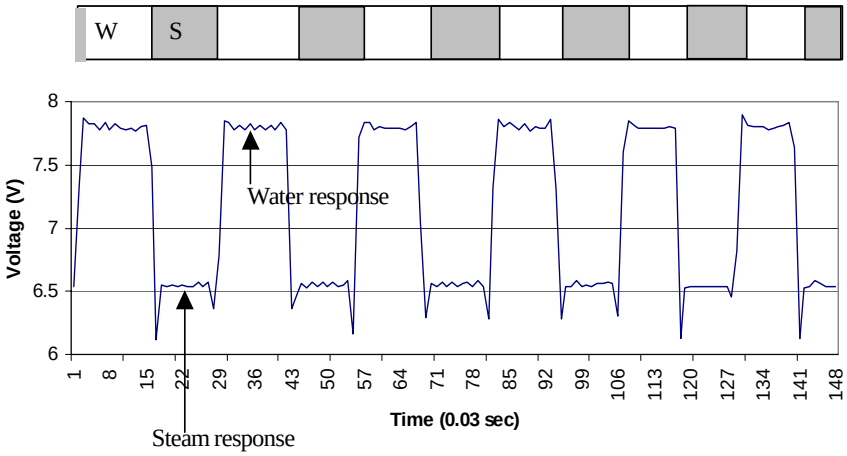

Figure 1.9: The signal of steam and water detected from fractional flow ratio detector.

Once the steam and water responses are obtained from the FFRD, the statistical histogram is plotted and the steam and water phase flow ratios are obtained by determining the threshold of the histogram. This is shown in Figure 1.10 and Table 1.1.

Table 1.1: The analysis results of steam and water fractional flow ratios from Figure 1.9.

Bin	*Frequency*	Discrimination
6.2	287	Steam
6.4	603	Steam
6.6	7021	Steam
6.8	600	Steam
7	110	Steam
7.2	20	Threshold
7.4	146	Water
7.6	400	Water
7.8	3810	Water
8	3462	Water
More	0	

Steam Total	8631
Water Total	7828
Grand total	16459

Fractional flow	
Steam	0.5243939
Water	0.4756061

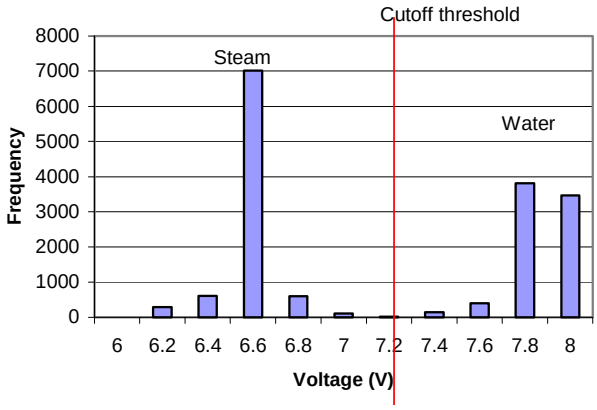

Figure 1.10: The histogram obtained from Figure 1.9.

The diameter of the FFRD tubing plays an important role in the accuracy of the f_w measurement under low f_w conditions. Here, we exam the effect of the FFRD tubing's size by using two different diameter of FFRD tubing.

First, a wider transparent glass tubing (3 mm OD, 1.4 mm ID) was installed. A new, high-speed data acquisition board (NI PCI-6023E) was also installed in the data acquisition computer. This replacement increased the data logging frequency from 50Hz to 250Hz. The calibration of water-phase flow ratio is shown in Figure 1.11. Though this replacement improved the f_w detection limit of the FFRD from 0.01 to around 0.005, f_w values show erratic and inconsistent behavior when f_w is less than 0.005, as shown in Figure 1.11(b). In order to find the solution to this problem, we observed the actual flow phenomena through the FFRD tubing, and did a preliminary classification of flow patterns correspond to logged FFRD signals. Flow patterns inside the FFRD tubing can be classified into four phenomena. With the increasing of the gas rate, the four phenomena are: segment flow, mostly segment flow, mostly droplet flow, and droplet flow. Cartoons of these four flow patterns are shown in Figure 1.12. The FFRD signals obtained from these four patterns are shown in Figure 1.13.

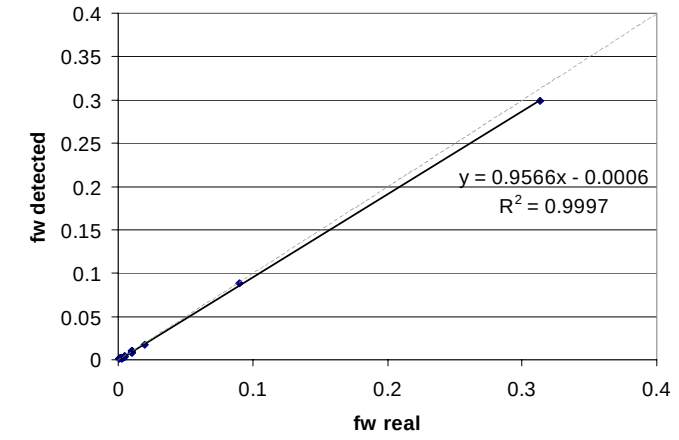

(a)

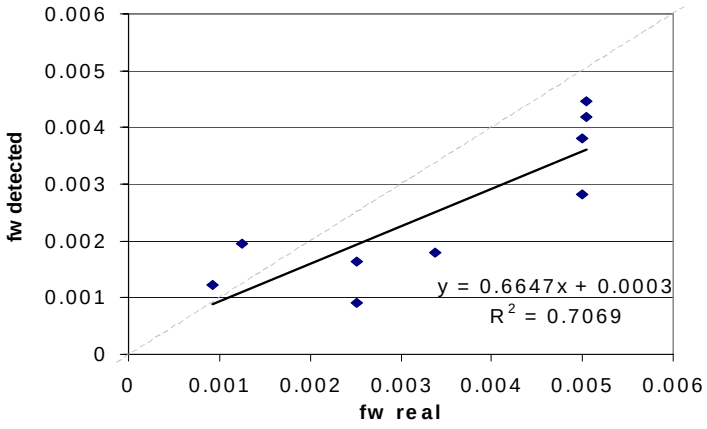

(b)

Figure 1.11:FFRD calibration with tubing ID: 1.4mm, (a) large scale, (b) small scale.

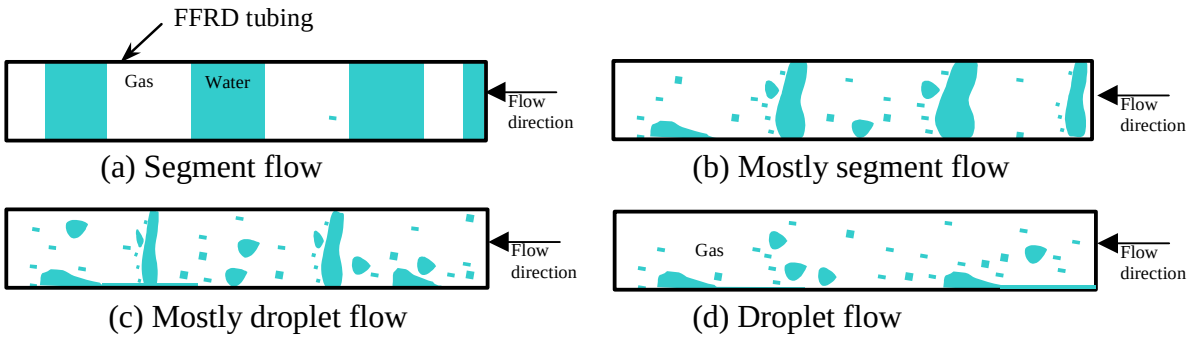

Figure 1.12: Flow pattern cartoons observed from FFRD tubing, (a) segment flow signal, (b) mostly segment flow signal, (c) mostly droplet flow signal and (d) pure droplet flow signal.

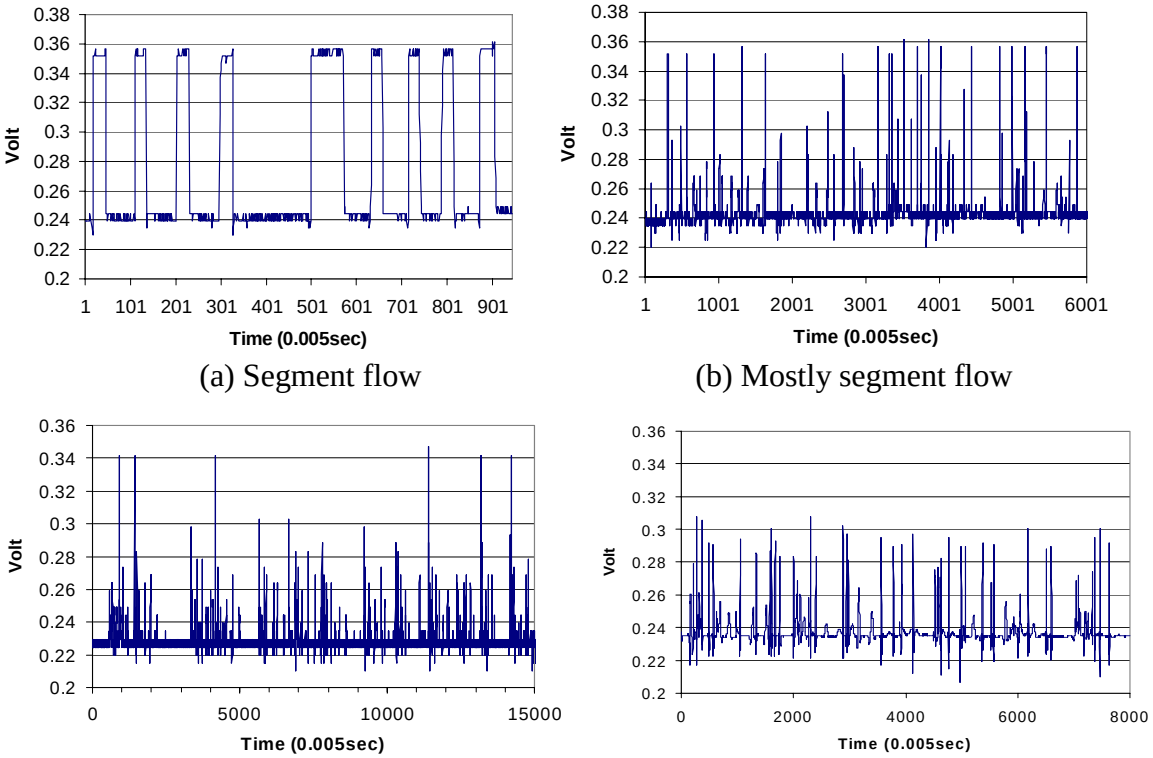

Figure 1.13: FFRD signals correspond to flow patterns shown in Figure 1.12, (a) segment flow signal, (b) mostly segment flow signal, (c) mostly droplet flow signal and (d) pure droplet flow signal.

After analyzing all the FFRD signals obtained by using the 1.4mm ID FFRD tubing, the approximate flow pattern map was drawn (Figure 1.14). Comparing Figure 1.14 and Figure 1.11, we discovered that when f_w is less than 0.005, the flow pattern turns to the pure droplet flow. The more the droplet flow, the more error would be obtained in FFRD detection. Droplets inside the tubing reflect and refract the light from the LCD source randomly, hence the signal attenuation becomes nonlinear. Figure 1.11(b) shows this inaccurate indication due to the droplet flow.

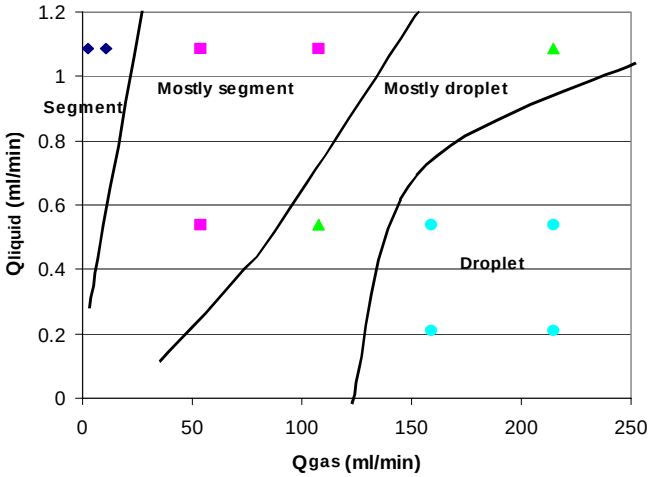

Figure 1.14: Flow pattern map developed from FFRD signal response by using 1.4mm FFRD tubing.

The major factor that controls the flow pattern is FFRD tubing diameter. To avoid the droplet flow, a narrower tubing could be used; however, the narrower the tubing, the more pressure drop throughout the FFRD and the more capillary effect. To maintain an appropriately small pressure drop, keep the tubing size small, and minimize the capillary effect, a new FFRD tubing with 1mm inner diameter and wide-open ends was redesigned to replace the original FFRD tubing (1.4mm) to achieve more segment flow instead of droplet flow inside the FFRD tubing under high flow rates. The schematic of this bell-end tubing is shown in Figure 1.15.

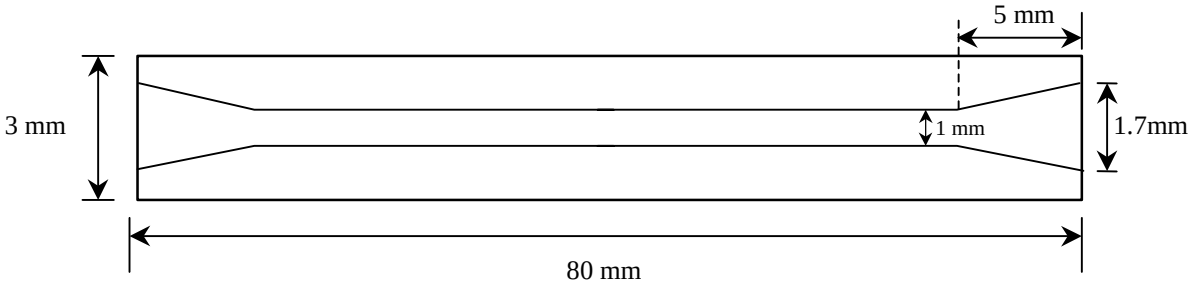

Figure 1.15: Bell-end FFRD tubing (ID=1.0mm, OD=3.0mm, Length=80mm)

The same high-speed data logging program which could reach 250Hz logging frequency was used. Also a more stable DC power supply was installed to avoid signal drift and fluctuation. The new calibration of the FFRD with all the improvements is shown in Figure 1.16 and the new flow pattern map obtained from FFRD signals in different phase-rate ratios is shown in Figure 1.17. Comparing Figure 1.16(b) with Figure 1.11(b), a more accurate measurement of fractional flow in two-phase flow is achieved. This improvement can be explained easily by comparing the flow pattern map in Figure 1.17 with that in Figure 1.14. There is no pure droplet flow region by using this narrower tubing. This increases the accuracy of FFRD logging.

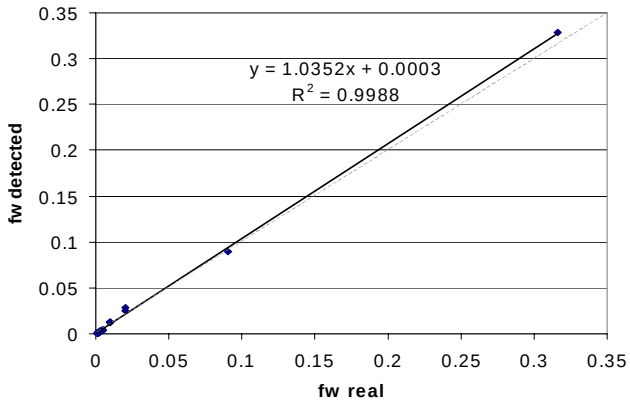

(a)

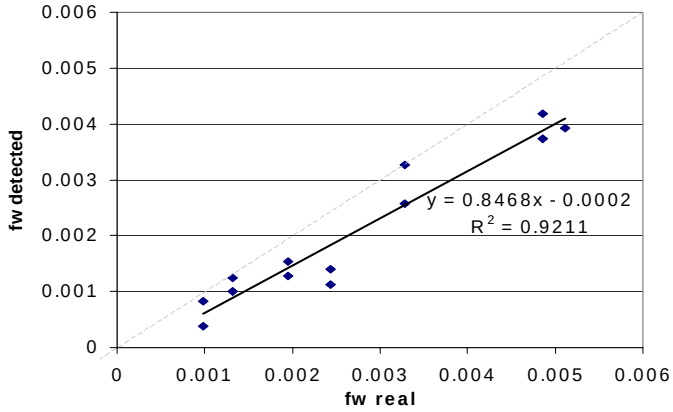

(b)

Figure 1.16:FFRD calibration with tubing ID: 1.0mm, (a) large scale, (b) small scale.

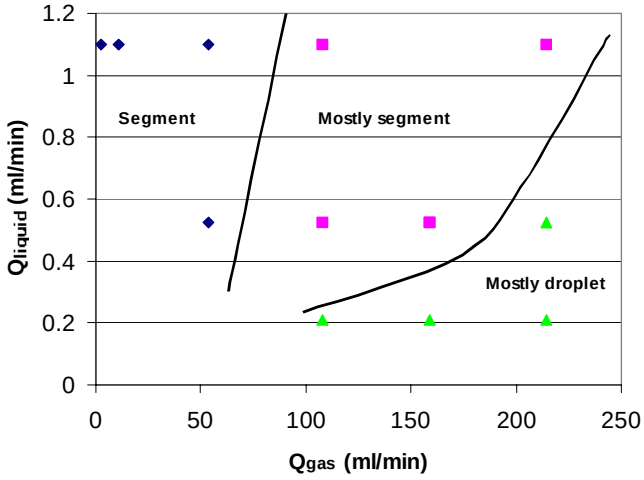

Figure 1.17: Flow pattern map developed from FFRD signal response by using 1.0mm, bell-end FFRD tubing.

1.4 CONTROL AND MEASUREMENT TECHNIQUES

There are two methods available to produce steam-water flow inside the fracture. One method is by injecting steam and water separately into the apparatus. The steam would be produced using a steam generator inside the air bath to boil steam from deaerated water. The other method is by injecting only deaerated water into the apparatus, after which the steam phase is produced by adjusting either pressure or temperature in the fracture. Since the steam quality from the steam generator is hard to control, the heat loss from the steam generator to the fracture apparatus is hard to determine, and there is a significant phase transformation at the moment when the injected steam and water meet in the inlet port, the latter method was used in this experiment.

The two factors that control the steam production are temperature and pressure. According to experience, adjusting pressure requires less equilibration time than adjusting temperature. To facilitate pressure adjustment, a physical back-pressure device was connected to the outlet of the apparatus to constrain the pressure inside the fracture to a specific value. For water, a meter pump (Dynamax, SD-200) controlled the rate of injection. The water used in the experiment needs to be deaerated almost completely. To reach this quality, distilled water was evacuated using a vacuum pump for 2 hours, and then the water was boiled to achieve a low dissolved-gas condition. This distilled, deaerated water was used as the injection fluid. Figure 1.18 shows a schematic diagram of this configuration.

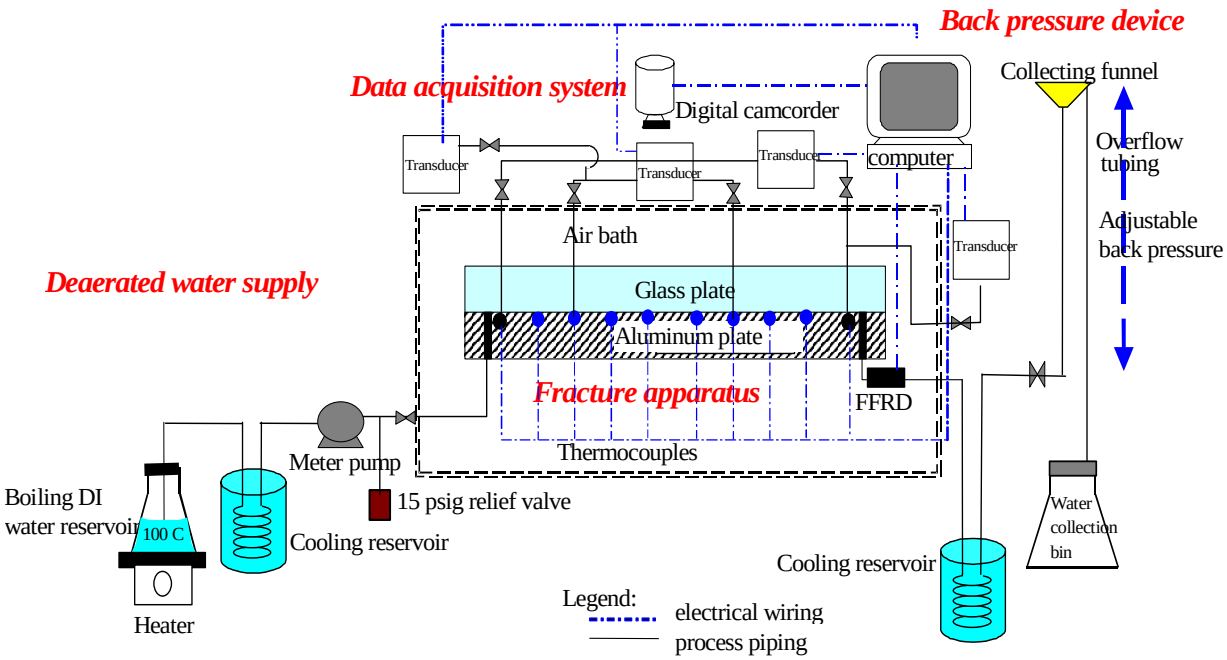

Figure 1.18: Process flow diagram for steam-water experiment.

Flow rates, q_w and q_s

For steam and water rates measurement, the fractional flow ratio detector (FFRD) was used to measure the outlet steam and water fractional flow ratio, f_s and f_w.

$$f_s = \frac{q_{out,s}}{q_{out,t}} \tag{1.18}$$

$$f_w = \frac{q_{out,w}}{q_{out,t}} \tag{1.19}$$

where $q_{out,s}$ is the output steam flow rate, $q_{out,w}$ is the output water flow rate, and $q_{out,t}$ is the output total flow rate. Once f_s and f_w are obtained, it is easy to evaluate $q_{out,s}$ and $q_{out,w}$ by using mass balance if a steady-state condition is reached. In order to catch the fast and unsteady steam and water segment in the outlet tubing, The FFRD was connected to the SCXI-1000 data acquisition device incorporating NI PCI-6023E, high-speed DAQ board, which can reach 250Hz maximum sampling frequency.

Once fractional flows are known, the steam and water flow rate can be calculated according to the mass balance under the assumption of steady state. The mass balance equation is:

$$m_{in} = q_{in,t}\rho_{w,at104^o c} = m_{out} = m_{out,w} + m_{out,s} = q_{out,t}(f_w\rho_{w,at104^o c} + f_s\rho_{s,at104^o c}) \tag{1.20}$$

where, m_{in}, m_{out} stand for the input and output mass, $q_{in,t}$ and $q_{out,t}$ stand for input and output volumetric flow rates, ρ is the density, and f_s and f_w are steam and water fractional flows.

If f_s and f_w are known from FFRD data, the total output flow rate, $q_{out,t}$, can be obtained from Eq. 1.20:

$$q_{out,t} = \frac{m_{in}}{f_w\rho_w + f_s\rho_s} \tag{1.21}$$

The end-point steam and water flow rates are:

$$q_{out,w} = f_w q_{out,t} = f_w \frac{m_{in}}{f_w\rho_w + f_s\rho_s} \tag{1.22}$$

$$q_{out,s} = f_s q_{out,t} = f_s \frac{m_{in}}{f_w\rho_w + f_s\rho_s} \tag{1.23}$$

Since the flow rates obtained are end-point flow rates, they can represent true flow rates under steady-state conditions. If the flow is in an extremely unsteady state, some mixed phase response will occur in the FFRD, and the flow rates calculated will become incorrect. However, if the flow is in quasisteady state (i.e. the steam or water flow rate increases at a fairly slow rate), flow rates obtained by this method should approximate the real flow rates except for a short delay of the phase response.

Saturation

Still images were extracted from digital video recorded during experiments. The data gathered from the video were correlated with the Labview data through the time read from the LCD monitor. Figure 1.19 shows a typical video image taken from the experiments.

From the still image shown in Figure 1.19, saturation was computed by measuring the area that each phase occupied. The photographs were processed in a Matlab® program. The program first cuts the photograph to display just the image of the flow area. Using this cut image, the program does quadratic discriminant analysis (QDA) to group the pixels of the picture into three groups: the water phase, steam phase and the frame. The grouping is based on color differences. Saturation is calculated as total pixels of the liquid group over the sum of the steam and liquid groups. Figure 1.20 is a gray-scaled image produced by the QDA program from the original cut photograph (Figure 1.19). The accuracy of the program in calculating the saturation can be related to the similarity in details of the gray scale image to the true image. From the figure, it can be said that the program has good accuracy.

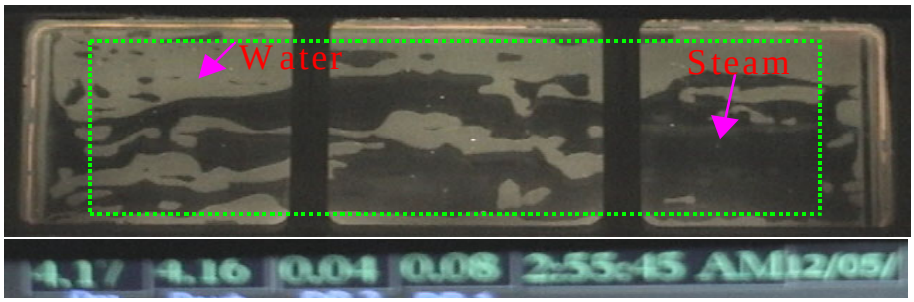

Figure 1.19: Sample video image taken for steam-water runs.

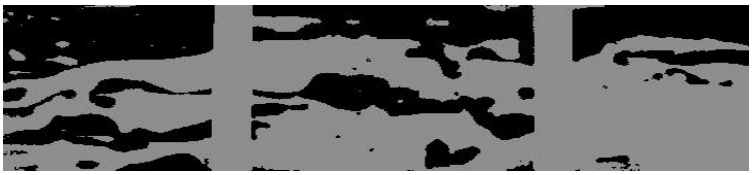

Figure 1.20: Processed gray scale image used in measuring saturation.

Pan et al. (1996) also used this technique for measurement of saturation. This study noted that the sources of error in this technique were the quality of the photographs and the water film adsorbed on the surfaces of the plates with the latter being of minimal effect. Good quality photographs are the ones with clear distinction between the gas and liquid phase. Good lighting is necessary so that the colors in the image come out clearly. The lighting should also be positioned in a way that it does not produce shadow on the flow area. The program will mistakenly take the shadow as steam phase even if there is liquid.

According to the nitrogen-water experiments by Diomampo (2001) and others, these fracture flow experiments are not expected to reach a perfect steady state. Instead, they are unsteady by nature. There are significant pressure fluctuations accompanied by saturation changes and the gas and liquid flow rates vary. Due to this behavior, the data acquisition task requires frequent gathering of instantaneous pressure, flow rate and saturation values. Instantaneous gathering of data was accomplished by the use of the digital video camcorder. Video shots were taken of the pressure, time and saturation data displayed all at the same time. Pressure and temperature data and related time were displayed by the LCD monitor connected to the computer, which also ran the data acquisition system. The

saturation was computed from the image of the whole flow area of the fracture. The methodology used to integrate all the data and signals and then calculate the steam-water relative permeabilities is illustrated in the flow chart in Figure 1.21.

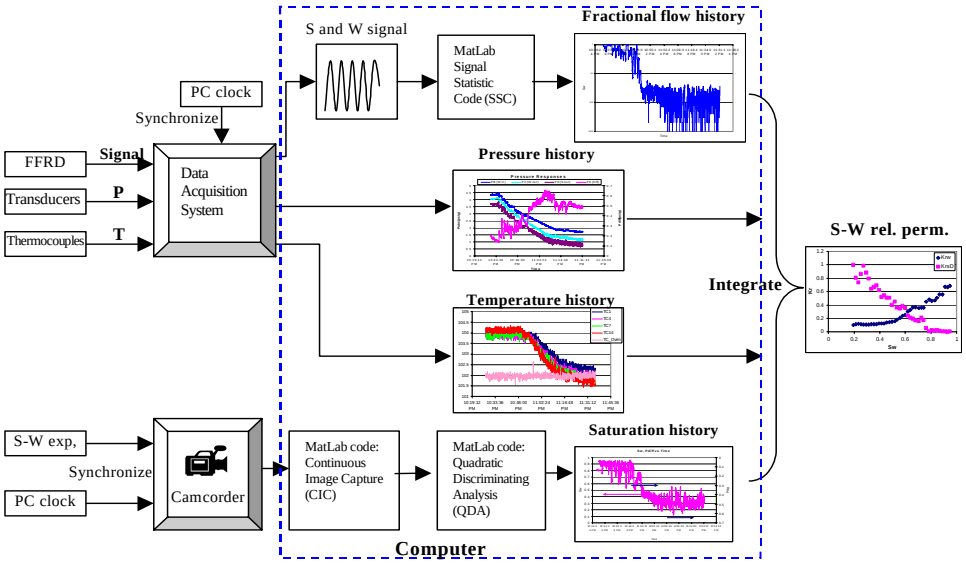

Figure 1.21: Data and signal processing flowchart.

1.5 STEADY-STATE EXPERIMENTAL RESULTS

Steady-state nitrogen-water experiment at room temperature

A steady-state nitrogen-water relative permeability experiment was conducted under a 24^{o}C environment. Before the experiment, the absolute permeability of the smooth-walled fracture was measured. As can be seen in Figure 1.22, with the 0.013cm fracture aperture, the absolute permeability of the fracture measured is around 1300 darcies when the back pressure is less than 2 psig. While applying the cubic law from Eq. 1.3, the permeability estimated is around 1400 darcies. This is close to our measurement. Figure 1.23 illustrates one run of this steady-state experiment. Input rates of water and gas were 10 *ml/min* and 50 *ml/min* respectively. Clearly, unlike in porous media, even though constant gas and water rates were input to the fracture, the water saturation kept fluctuating in the fracture and the instantaneous f_w sensed from the FFRD followed this saturation fluctuation as shown in the top plot of Figure 1.23. The corresponding pressure response was also recorded as shown in the bottom plot of Figure 1.23. The gas-water flow in the fracture was unstable.

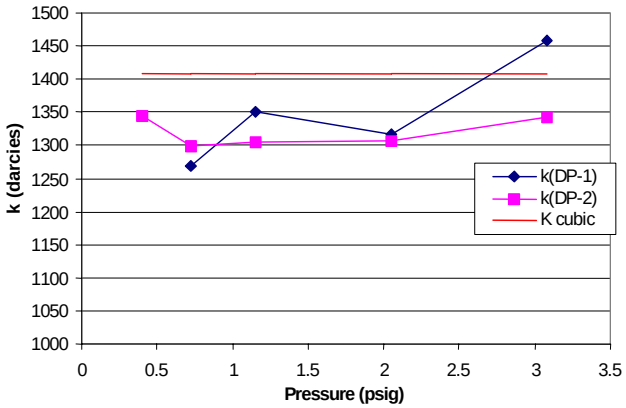

Figure 1.22: Absolute permeability of the fracture (aperture = 0.013cm) at 24^{o}C with different back pressures.

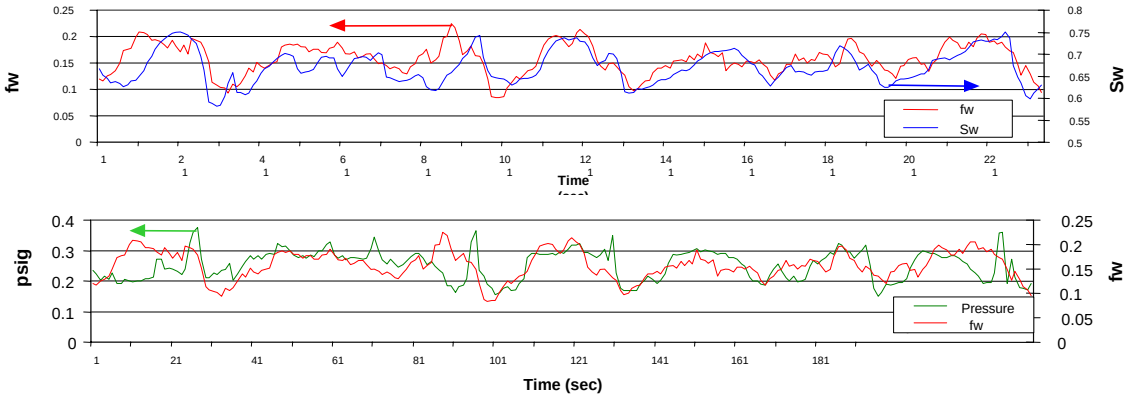

Figure 1.23: the relationship among water saturation, water fractional flow and pressure difference along the fracture at rates of Qw=10ml/min, Qg=50ml/min.

More than 3000 still images were extracted from the digital video and used for the flow pattern characterization and saturation calculation. Several types of flow patterns observed under high, intermediate, and low water saturation are shown in Figure 1.24, 1.25 and 1.26 respectively. Each figure shows four consecutive images. Figure 1.24 shows the nitrogen-water flow under high water saturation. Nitrogen moves in narrow slugs and flows discontinuously because of the relatively low gas flow rate. The higher pressure drop happens mostly when a slug tries to break through the water region (right images). Once the slug reaches the outlet of the fracture, the pressure drop decreases. This type of slug movement was seen frequently in high water saturation situations. Figure 1.25 shows the nitrogen-water flow at intermediate water saturation. Unlike the high water saturation case, the gas forms its own flow path through the fracture and gas and water behave nearly like layer flows under intermediate water saturation. Most of the gas flows in the upper region of the fracture, while most of the water flows in the lower. As can be seen in these four images, the gas flow path is stable. If a longer time scale is used to observe the behavior, some gas channels are seen to be blocked, and some are seen to be unblocked by water. In other words, the gas flow path undergoes continuous snapping and reforming due to the invasion of water. These pictures were taken at a gas rate of 200 ml/min and water rate of 2 ml/min. Figure 1.26 shows the nitrogen-water flow under low water saturation. In this gas-

dominated case, water flows through some narrow paths and sometimes as slow slugs as shown in the figure. The pressure drop along the fracture is fairly stable in this condition.

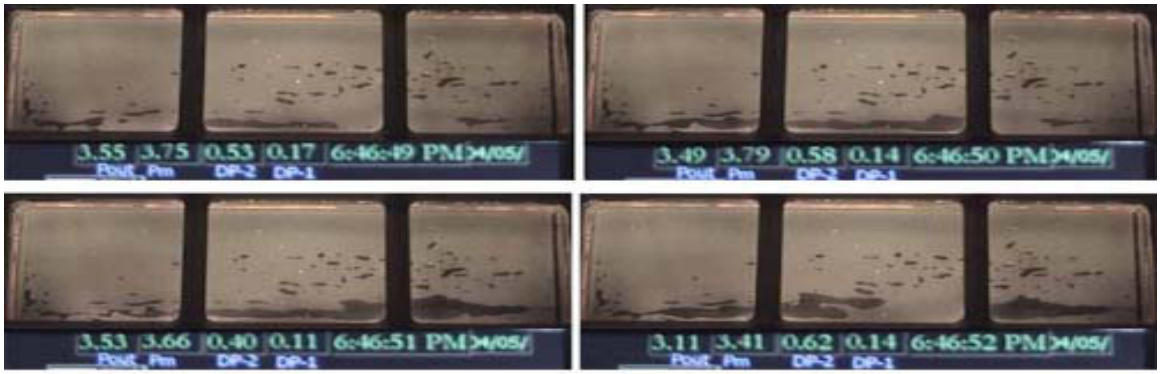

Figure 1.24: The continuous nitrogen-water flow behavior in smooth-walled fracture at room temperature under high water saturation (~90%) (nitrogen phase is dark, water phase is light, Qw=10ml/min, Qg=5ml/min).

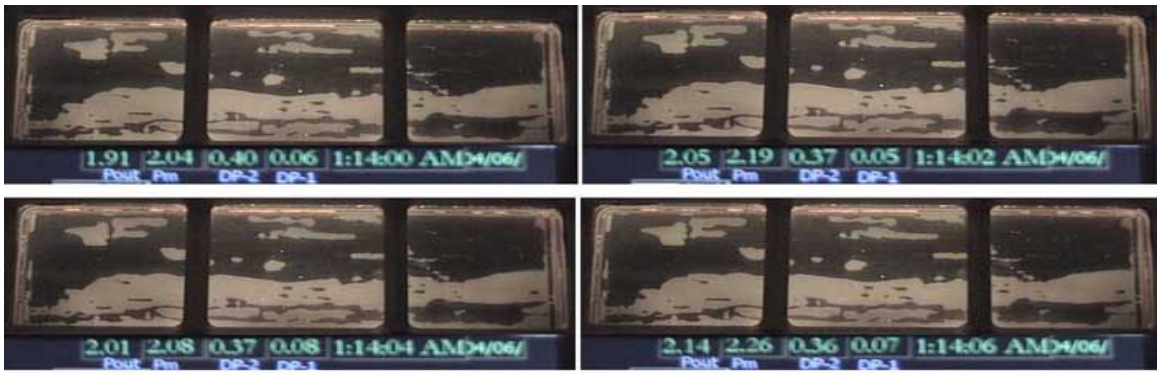

Figure 1.25: The continuous nitrogen-water flow behavior in smooth-walled fracture at room temperature under intermediate water saturation (~40%) (nitrogen phase is dark, water phase is light, Qw=2ml/min, Qg=200ml/min).

Figure 1.26: The continuous nitrogen-water flow behavior in smooth-walled fracture at room temperature under low water saturation (~15%) (nitrogen phase is dark, water phase is light, Qw=0.5ml/min, Qg=200ml/min).

Steady-state, nitrogen-water relative permeabilities at room temperature (24^{o}C) over these more than 3000 data points were calculated and are shown in Figure 1.27. Window averages over the 2% saturation range from those comprehensive points are also shown in

the same figure. Comprehensive water relative permeabilities are scattered under high water saturation owing to the slug flow in gas phase as shown in Figure 1.24. The vertical scattered effect in the gas relative permeabilities under extremely low water saturation may be associated with either the pressure fluctuation due to the slow moving water slugs as shown in Figure 1.26 or the difficulty in sensing the instantaneous f_w from the FFRD at low f_w. The average nitrogen-water relative permeabilities show good linearity in water values. Gas curves are more convex compared to the water values. Essentially, the average relative permeability curve shows less phase interference compared to the general relative permeability curves in porous media (Corey-type curves).

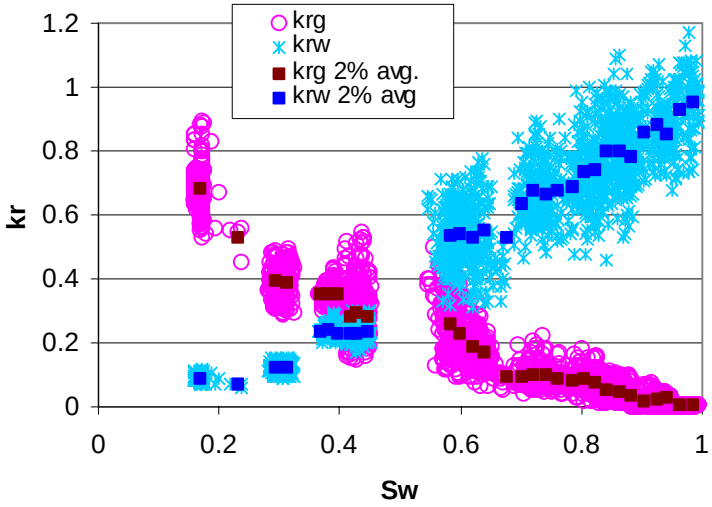

Figure 1.27: Comprehensive steady-state nitrogen-water relative permeabilities in the smooth-walled fracture at room temperature and their 2% window averages.

Steady-state nitrogen-water experiment at high temperature

The steady-state high-temperature nitrogen-water relative permeability experiment was conducted under a 90^{o}C environment. Before the experiment, the absolute water permeability was measured. As shown in Figure 1.28, with 0.013cm fracture aperture, the absolute permeability of the fracture measured is around 1300 darcies. This result is close to that in the room temperature case. Therefore the absolute permeability appears to be insensitive to the temperature over the range from 24 to 90^{o}C. While using the cubic law from Eq. 1.3, the permeability estimated is around 1400 darcies. This is close to our measurement.

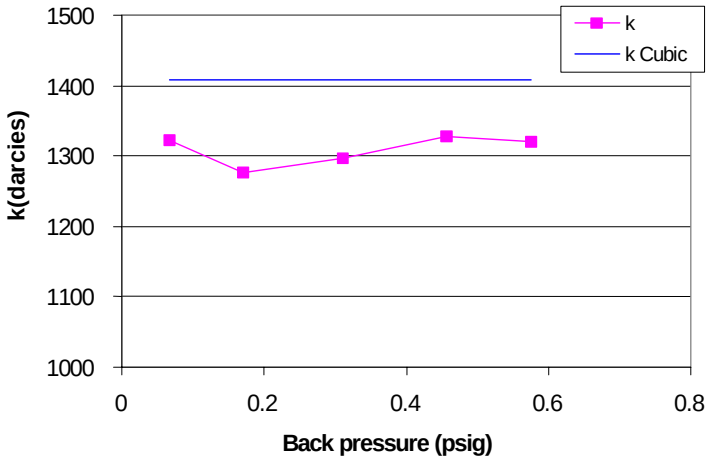

Figure 1.28: Absolute permeability of the fracture (aperture = 0.013cm) at 90^{o}C with different back pressures.

As in the room temperature experiment, several types of flow patterns were observed under high, intermediate, and low water saturation as shown in Figures 1.29, 1.30 and 1.31 respectively. Each figure shows four consecutive images taken over either one or two second periods. Figure 1.29 shows the nitrogen-water flow under high water saturation. The flow regime under this condition is similar to that at room temperature (Figure 1.24). Nitrogen moves as narrow slugs and flows discontinuously because of the relatively low gas rate. Also more immobile water saturation is seen in Figure 1.29 in comparison to Figure 1.24.

Figure 1.30 shows the typical nitrogen-water flow behavior under intermediate water saturation. Similar to the room temperature case, the gas forms very stable flow paths through the fracture and the gas and water behave like layer flows. Almost all of the gas flows solely in the center region of the fracture, while most of the water flows above and below the gas path. Except for a small amount of immobile water inside the central gas channel, the gas path is more uniform and is not tortuous. These images were taken at a gas rate of 150 *ml/min* and water rate of 7.5 *ml/min*.

Figure 1.31 shows the nitrogen-water flow under low water saturation. Comparing Figure 1.31 to Figure 1.26, it is clear that the water saturation is much smaller than that in the room temperature case (Figure 1.26) when input rates are the same (Qw=0.5*ml/min* and Qg=200*ml/min* in both cases). The instantaneous f_w sensed was also smaller than that in room temperature case. Consequently, some water evaporated into gas phase during the two-phase flow due to the high temperature and relatively large gas flow rate. It is necessary to evaluate the evaporation rate and the steam ratio in the gas phase since the gas phase contains not only nitrogen but also some amount of water vapor in this high-temperature case.

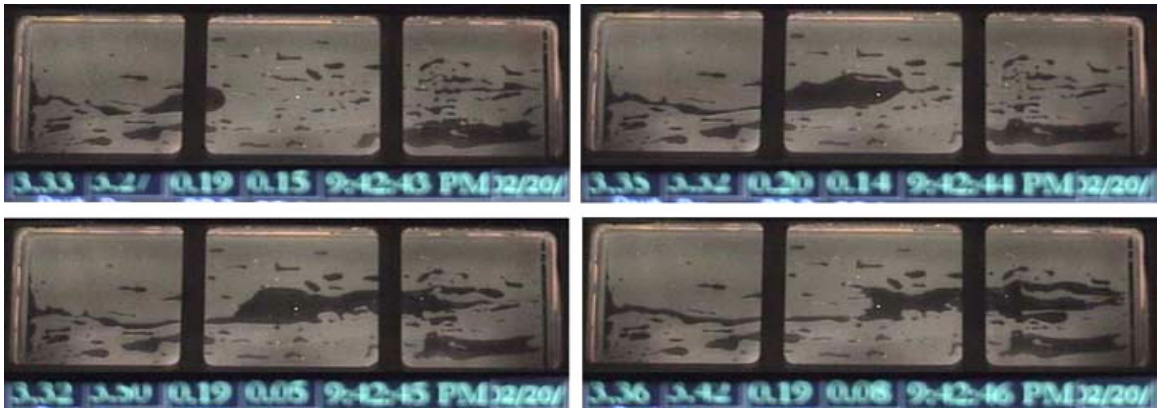

Figure 1.29: The continuous nitrogen-water flow behavior in smooth-walled fracture at high temperature (90^{o}C) under high water saturation (>80%) (nitrogen phase is dark, water phase is light, Qw=10ml/min, Qg=5ml/min).

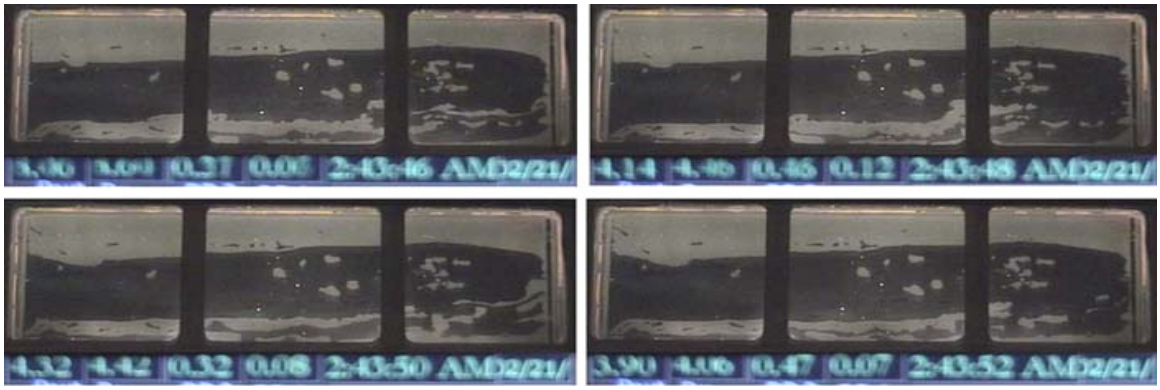

Figure 1.30: The continuous nitrogen-water flow behavior in smooth-walled fracture at high temperature (90^{o}C) under intermediate water saturation (~40%) (nitrogen phase is dark, water phase is light, Qw=7.5ml/min, Qg=150ml/min).

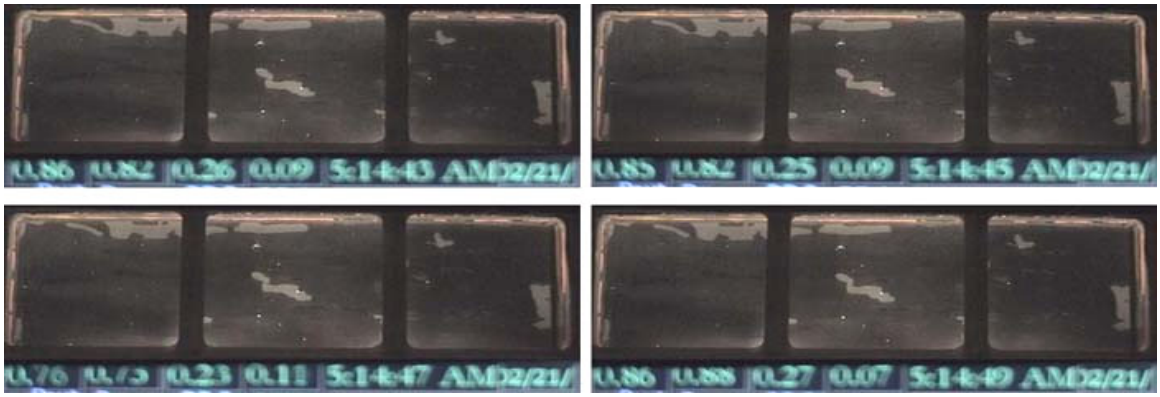

Figure 1.31: The continuous nitrogen-water flow behavior in smooth-walled fracture at high temperature (90^{o}C) under low water saturation (~5%) (nitrogen phase is dark, water phase is light, Qw=0.5ml/min, Qg=200ml/min).

The water evaporation rate can be evaluated by using the FFRD measurements. Instantaneous f_w obtained from the FFRD can be used to calculate evaporation rate, X, given input water and gas (nitrogen) rates. By using the mass balance theory, X can be calculated by Eq. 1.24:

$$X = \frac{Q_{w0} - f_w(Q_{w0} + Q_{go})}{1 + f_w(\frac{v_s}{v_w}) - f_w} \tag{1.24}$$

where, Q_{w0} and Q_{g0} are the input water rate and gas rate respectively; v_w and v_s are the specific volume for water and steam at some specific temperature; f_w is the instantaneous water fractional flow measured by the FFRD. The evaporation rate evaluated from Eq. 1.24 with different gas rates in this high-temperature experiment is presented in Figure 1.32. Generally, the evaporation rate increases while the gas rate increases. Figure 1.33 shows the gas fractional flow, f_g, versus the steam ratio which is the volume of the steam evaporated from the water phase to the total volume of gas (sum of the input gas and produced steam). Most of steam ratios stay below 0.5 as f_g is less than 0.97. In extremely high f_g situations, i.e. gas rates are much larger than water rates, steam ratios increase gradually and reach a maximum value of 0.7.

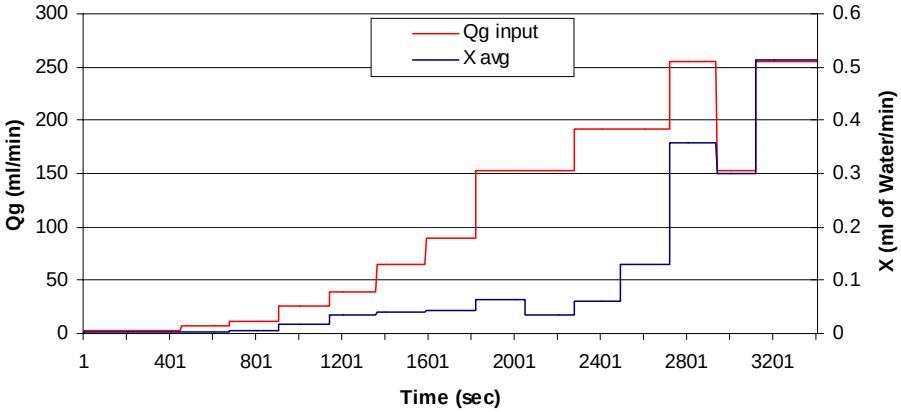

Figure 1.32: Water evaporation rates versus gas rates in the steady-state nitrogen-water experiment at 90°C.

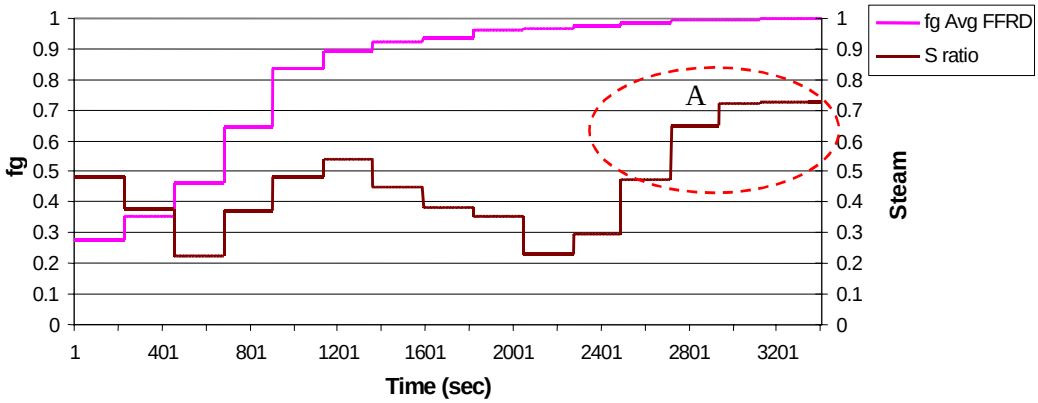

Figure 1.33: Steam ratios versus gas fraction flow in the steady-state nitrogen-water experiment at 90°C.

Comprehensive high-temperature nitrogen-water relative permeabilities obtained from over 3000 points are shown in Figure 1.34. The 2% window averages are also provided in the same figure. Generally, high-temperature nitrogen-water relative permeability values behave similar to the room temperature case (Figure 1.27) with the exception of low water

saturation cases where the gas-phase relative permeabilities in the high temperature case are greater then those at room temperature.

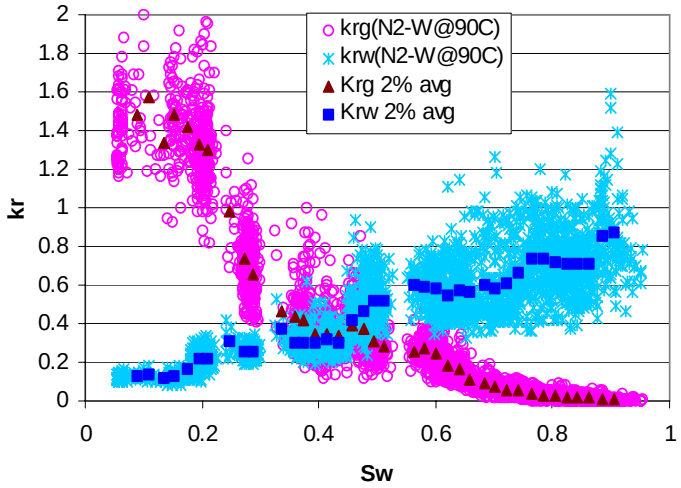

Figure 1.34: Comprehensive Steady-state nitrogen-water relative permeabilities in the smooth-walled fracture at high temperature (90^{o}C) and their 2% window averages.

Steady-state steam-water experiment

The steady-state steam-water experiment is in progress. Results are expected to be presented in the next report.

Unsteady Steam-Water Relative Permeability Experiment

The unsteady steam-water relative permeability experiment was conducted at around 104^{o}C. The procedure and detail of the unsteady steam-water relative permeability experiment were described in the previous quarterly report. The flow regime under high water saturation condition behaves similar to the nitrogen-water case. As can be seen in Figure 1.35, the steam phase flows in fast moving slugs. The shape of slugs is more amorphous than that in the nitrogen-water case.

The steam-water flow behavior is different from that of the nitrogen-water case under intermediate and low water saturations. As illustrated in Figures 1.36 and 1.37, the steam can flow via slugs, bubbles, and channels. On the other hand, the water flows via water slugs, water bubbles, and water channels. Even under the low water saturation conditions, the steam-water flow is still unstable. The steam phase and water phase can flow together in several different forms. This two-phase cocurrent flow situation was rarely seen in the nitrogen-water case.

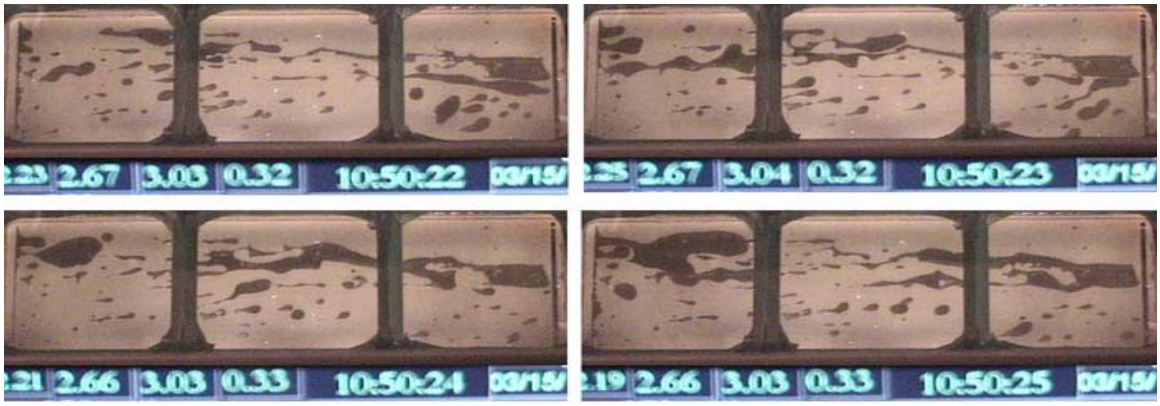

Figure 1.35: The continuous steam-water flow behavior in smooth-walled fracture under high water saturation (~90%). (steam phase is dark, water phase is light).

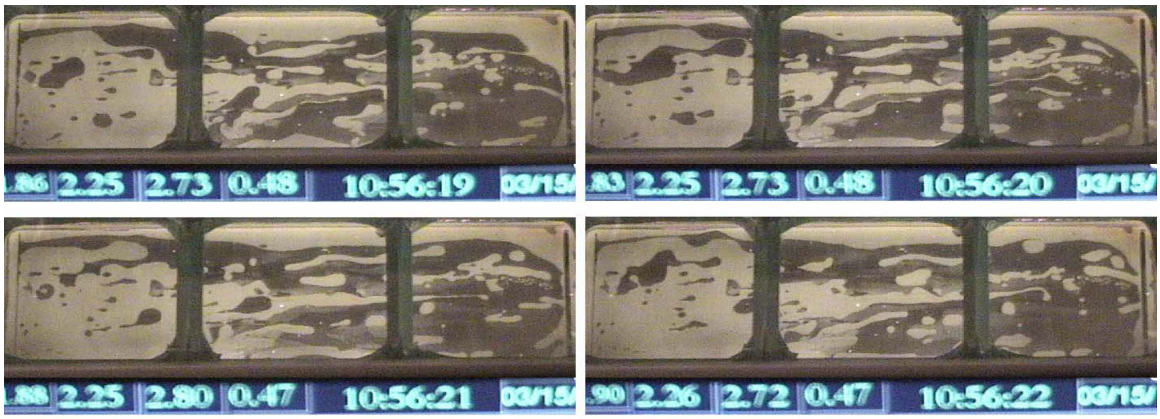

Figure 1.36: The continuous steam-water flow behavior in smooth-walled fracture under intermediate water saturation (~40%). (steam phase is dark, water phase is light).

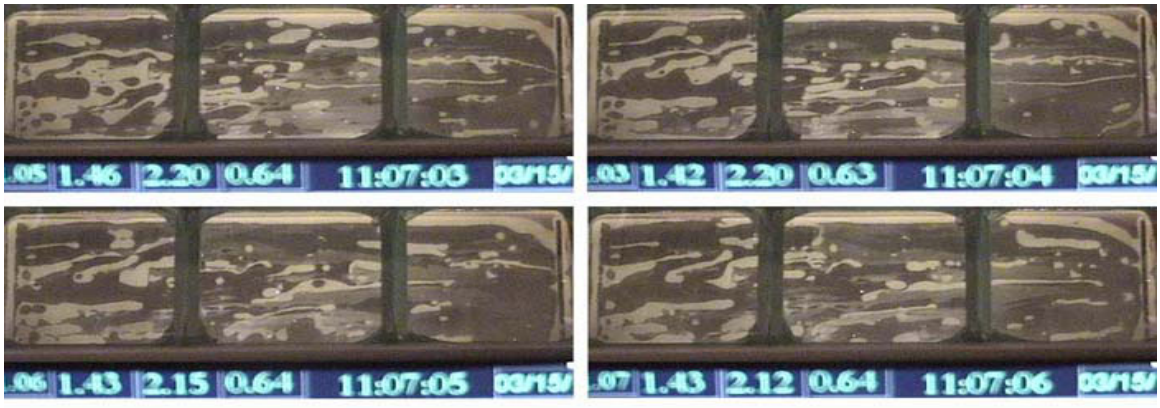

Figure 1.37: The continuous steam-water flow behavior in smooth-walled fracture under low water saturation (<20%). (steam phase is dark, water phase is light).

Figure 1.38 shows the unsteady experiment result. The k_{rw} values behave smoothly, whereas the k_{rs} values are scattered. As mentioned before, this scattered effect could be associated partly with the steam and water flow-rate measurement error but seems to be caused more prominently by the fluctuating nature of the flow. The detail of this error is due to the delay of f_s and f_w measurement from the FFRD and the measurement error

caused by the extremely high-speed steam flow which collapses the water component into many tiny water drops that are hard to detect in the FFRD. This will lower the measurement accuracy significantly.

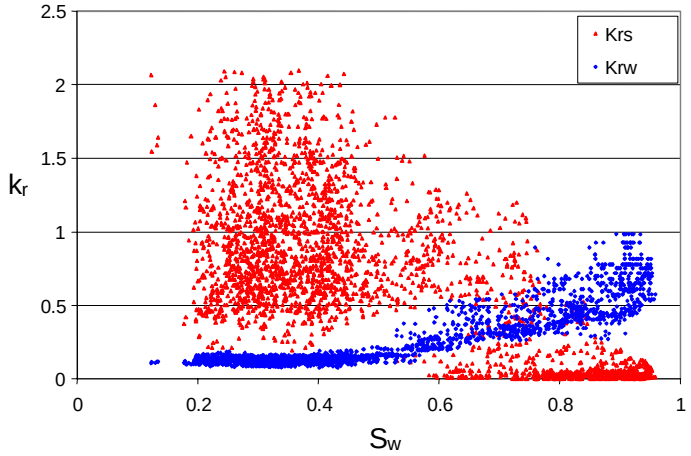

Figure 1.38: Comprehensive steam-water relative permeabilities in the unsteady experiment.

Further processing was applied to Figure 1.38 to characterize the steam-water flow behavior. Figure 1.39 was obtained by averaging the relative permeability over 2% saturation ranges from Figure 1.38. The figure shows good correlation in both steam and water curves. What is interesting is that the sum of these two curves is close to one, which indicates less phase interference. This result is different from the nitrogen-water case which showed a near Corey-type relative permeability behavior.

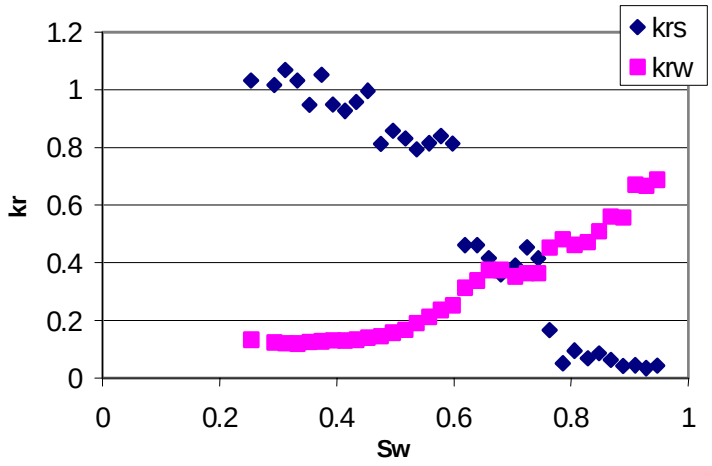

Figure 1.39: Steam-water relative permeabilities in the unsteady experiment by using 2% S_w averages.

1.6 DISCUSSION

Comprehensive nitrogen-water relative permeabilities at room (24°C) and high temperature (90°C) are shown in Figure 1.40. Data points from room temperature and high temperature cases show acceptable correlation. Figure 1.41 shows moving window averages of the full results shown in Figure 1.40. Generally, relative permeability values at these two different

temperatures are close when the water saturation is greater than 0.5 (which is water-dominated condition). On the other hand, relative permeabilities at 90°C have higher values than those at 24°C when water saturation is less than 0.5 (which is gas-dominated condition). Particularly, the gas-phase relative permeability values at 90°C show a more significant increasing trend in comparison to the case of 24°C (part A, Figure 1.41). This difference might be attributable to the increase of the steam ratio as shown in Figure 1.33. In the high-temperature, nitrogen-water experiment, water can evaporate to the vapor phase, especially in a high gas rate situation. As shown in part A in Figure 1.33, when gas fractional flow, f_g, is close to 1, the steam ratio reaches 0.73. This corresponds to part A in Figure 1.41. This indicates that the more water vapor in the gas phase, the higher the gas-phase relative permeability values.

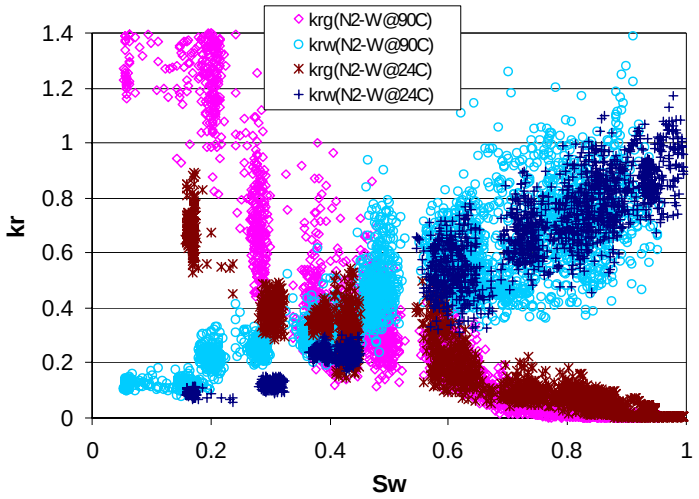

Figure 1.40: Comparison of comprehensive nitrogen-water relative permeabilities between 90°C and 24°C in the smooth-walled fracture.

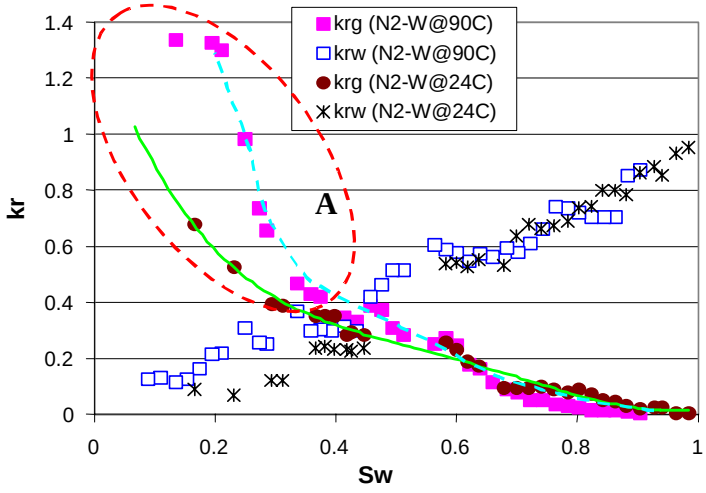

Figure 1.41: Comparison of average nitrogen-water relative permeabilities between 90°C and 24°C in the smooth-walled fracture.

The comparison of comprehensive relative permeabilities between steam- and nitrogen-water cases in the smooth-walled fracture is shown in Figure 1.42. Water-phase relative

permeability values show similar behavior in all these three cases. For the gas-phase relative permeability values, although the steam-phase values are scattered they are much higher than the nitrogen-phase values. This indicates that steam-phase flow encounters less phase interference than nitrogen-phase flow. Steam-water results were obtained from the unsteady experiment; therefore, more errors and uncertainties were expected. This probably contributes partially to the scattered steam-phase values. The more stable and accurate, steady-state experiment is in progress. Figure 1.43 shows window averages through all values in Figure 1.42. The liquid curve in the steam-water case is lower than that in the nitrogen-water case, which might shows an inconsistency with some theoretical studies. Also steam-water case may lose some accuracy at low water saturation ranges because of the error from the FFRD. On the other hand, the gas curves behave very differently. The steam curve shows a much more mobile character than the nitrogen curve, which can be seen from the higher relative permeability values in the steam curve in Figure 1.43. This phenomenon was also observed from the digital images.

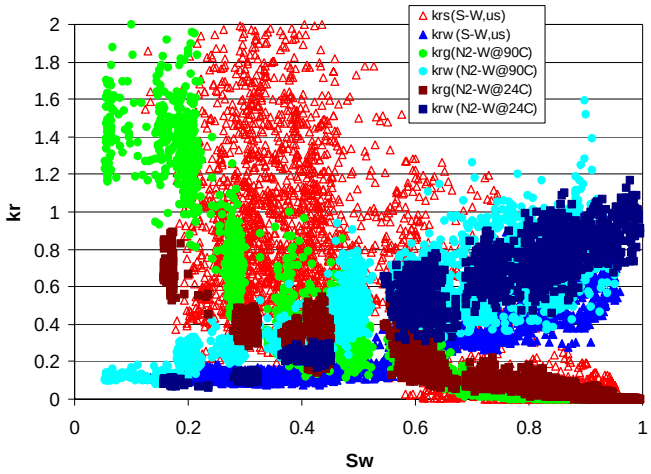

Figure 1.42: Comparison of comprehensive relative permeabilities between steam- and nitrogen-water cases in the smooth-walled fracture.

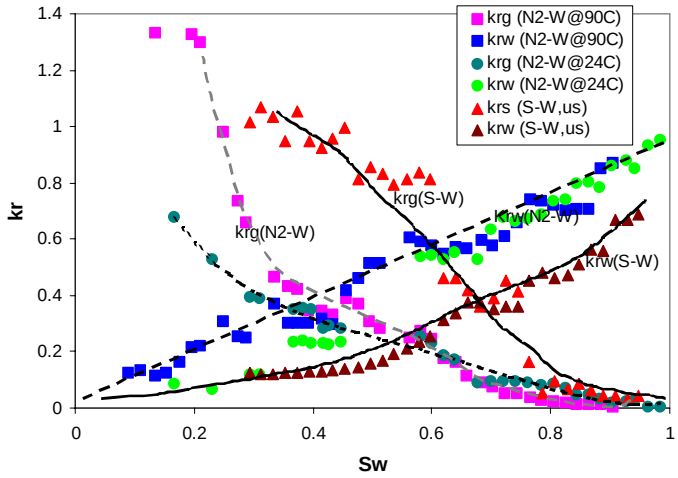

Figure 1.43: Comparison of relative permeability curves between steam- and nitrogen-water cases in the smooth-walled fracture.

Figure 1.44 summarizes the recent measurements of gas-water relative permeabilities in fractures in comparison to a collection of previously published results. Comparing the current results with previous measurements of air-water relative permeabilities in fractures, both steam- and nitrogen-water values from this research behave close to X-curve, which represents a behavior different from previous published measurements. Most of the previously published results proposed that air-water relative permeabilities in fractures follow the Corey-type curve or lie below it. It is necessary to mention that some of fractures in these studies were rough-walled. Currently, the roughness of the fracture was not been considered in this research. Furthermore, the steam-water results presented here are from the unsteady experiment. The steady-state, steam-water experiment are in progress. On the other hand, Romm (1966) also found similar X-curve behavior in his experiment with kerosene and water through an artificial smooth parallel-plate fracture lined with strips of polyethylene or waxed paper.

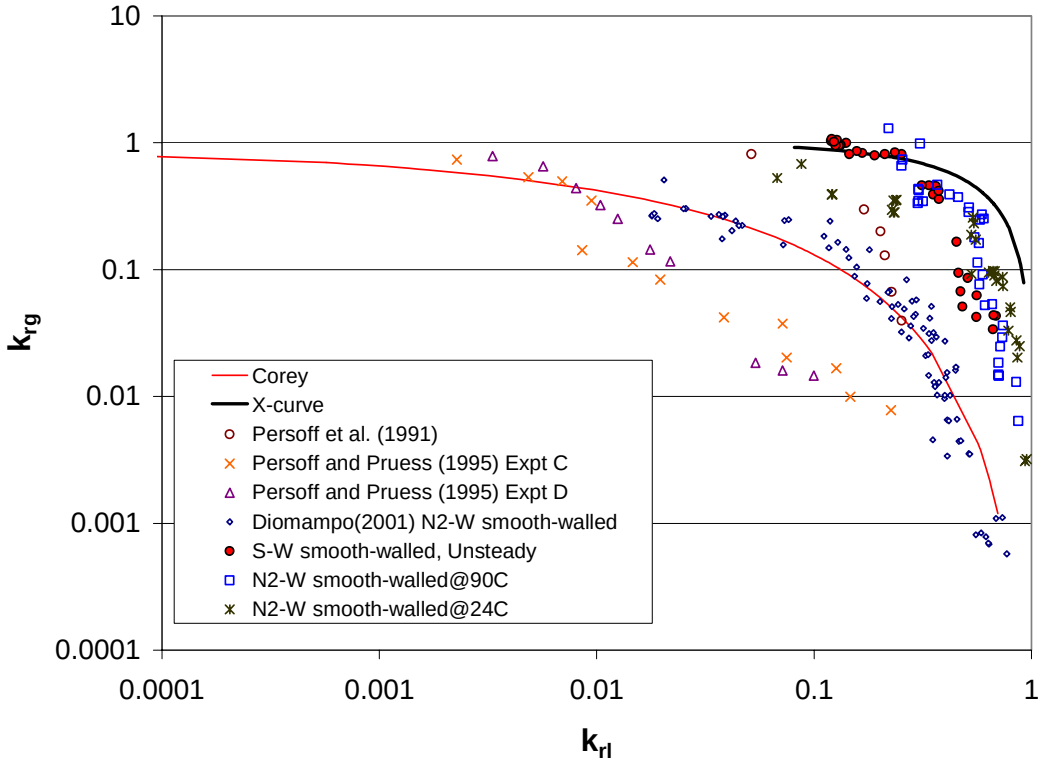

Figure 1.44: Comparison of steam- and nitrogen-water relative permeabilities in this research with previous measurements of air-water relative permeabilities in fractures.

2. A WETTABILITY EVALUATION METHOD FOR TWO-PHASE FLUID FLOW SYSTEMS

This research project is being conducted by Senior Research Engineer Kewen Li and Professor Roland Horne. The objective of this project is to develop a method of determining wettability in two-phase fluid flow, including steam-water systems.

2.1 SUMMARY

Methods to determine the wettability in both gas-liquid-rock and liquid-liquid-rock systems have been few. To this end, a method was developed to evaluate the wettability in both gas-liquid-rock systems and liquid-liquid-rock systems. The method can be used to evaluate the wettability at a specific wetting phase saturation if the capillary pressure and relative permeability at this fluid saturation are known. The validity of the proposed technique was tested qualitatively and quantitatively using experimental data of capillary pressure and relative permeability from different systems. The wettability index calculated using the proposed technique was greater in the drainage case than that in the imbibition case, which is reasonable and consistent with the present understanding. Results also showed that the wettability index calculated using the proposed method may or may not be independent of fluid saturation in the cases studied.

2.2 INTRODUCTION

Earlier (Li and Horne, 2002) we developed a method to infer the wettability of steam-water-rock systems based on the relationship between permeability and capillary pressure by Purcell (1949). In the current project we demonstrated using experimental data that the method could be suitable for both gas-liquid-rock and liquid-liquid-rock systems. The values of the wettability index were calculated in both drainage and imbibition processes using the experimental data of capillary pressure and relative permeability in different systems. To further verify the method we developed, experimental data from gas-oil-rock, gas-water-rock, oil-water-rock systems were also used. The calculated results were compared with the measured values of wettability index. The comparison provided evidence to the general validity of the proposed method to evaluate wettability.

2.3 THEORY

Li and Horne (2002) proposed a method to infer the wettability index of gas (steam)-water-rock systems. Theoretically this method can be suitable for both gas-liquid-rock and liquid-liquid-rock systems. The equation to calculate the wettability index is expressed as follows:

$$W_{iw} = \sqrt{\left(\frac{\lambda+2}{\lambda}\right)\left(\frac{k}{F\phi}\right)\left(\frac{k_{rw}}{S_w^*}\right)}\,\frac{P_c}{\sigma} \tag{2.1}$$

where W_{iw} is the wettability index at a specific wetting phase saturation; λ is the pore size distribution index; k and ϕ are the absolute permeability and porosity of the rock; F is the so-called lithology factor; σ is the interfacial tension between the two fluids; P_c and S_w^* are

the capillary pressure and the normalized saturation of the wetting phase;. k_{rw} is the relative permeability of the wetting phase.

The value of wettability index defined by Eq. 2.1 ranges from -1 to 1. Eq. 2.1 was derived according to the relationship between permeability and capillary pressure proposed by Purcell (1949). The derivation of Eq. 2.1 was presented in a previous paper (Li and Horne, 2002).

An important significance of Eq. 2.1 is that it may be possible to determine the wettability of gas-liquid-rock systems by using the data from a simple spontaneous water imbibition experiment. Because the relative permeability and the capillary pressure at a specific water saturation can be calculated simultaneously from one single spontaneous water imbibition test according to the method developed by Li and Horne (2001a), the wettability index may be obtained using Eq. 2.1.

Relative permeability can be inferred from capillary pressure data. There have been many models representing the relationship between relative permeability and capillary pressure. Eq. 2.1 can be reduced if such models are substituted into Eq. 2.1.

If the wettability of a fluid-rock system does not change with the fluid saturation, as is usually assumed, then $\sqrt{(\frac{k_{rw}}{S_w^*})}P_c$ should be constant according to Eq. 2.1. We will show in the following section that if the capillary pressure curve and the wetting phase relative permeability are represented using the Purcell model (1949), $\sqrt{(\frac{k_{rw}}{S_w^*})}P_c$ does not change with the fluid saturation. If other models such as the Corey (1954) or the Brooks-Corey (1966) models are used to calculate the wetting phase relative permeability from capillary pressure data, the results would be different. This may be verified using the data from simultaneous measurements of capillary pressure and relative permeability curves.

Based on the Purcell model, the wetting phase relative permeability can be calculated accurately using the following equation:

$$k_{rw} = (S_w^*)^{\frac{2+\lambda}{\lambda}} \tag{2.2}$$

Eq. 2.2 was derived by substituting the following capillary pressure model into the Purcell model (1949):

$$P_c = p_e (S_w^*)^{-1/\lambda} \tag{2.3}$$

where p_e is the entry capillary pressure. The normalized saturation of the wetting phase in drainage cases is calculated as follows:

$$S_w^* = \frac{S_w - S_{wr}}{1 - S_{wr}} \tag{2.4}$$

where S_w and S_{wr} are the specific saturation and the residual saturation of the wetting phase.

Substituting Eq. 2.2 into Eq. 2.1, one can obtain:

$$W_{iw} = \sqrt{(\frac{\lambda + 2}{\lambda})(\frac{k}{F\phi})}\,\frac{P_e}{\sigma} \tag{2.5}$$

According to Eq. 2.5, wettability does not change with the wetting phase saturation if the Purcell model (1949) is used to represent the relationship between relative permeability and capillary pressure. We reported the experimental data that support Eq. 2.5 in Li and Horne (2002).

The Brooks and Corey relative permeability model (1966) for the wetting phase is expressed as follows:

$$k_{rw} = (S_w^*)^{\frac{2+3\lambda}{\lambda}} \tag{2.6}$$

Substituting Eq. 2.6 into Eq. 2.1, the following equation can be obtained for the calculation of wettability index:

$$W_{iw} = \sqrt{(\frac{\lambda + 2}{\lambda})(\frac{k}{F\phi})}\,\frac{P_e}{\sigma} S_w^* \tag{2.7}$$

One can see from Eq. 2.7 that the wettability index is proportional to the normalized wetting phase saturation if the Brooks and Corey model is used to represent the relationship between relative permeability and capillary pressure.

Similarly, if the Corey model (1954) is used to represent the relationship between relative permeability and capillary pressure, the wettability index can be calculated as follows:

$$W_{iw} = \sqrt{2(\frac{k}{F\phi})}\,\frac{P_e}{\sigma} S_w^* \tag{2.8}$$

Eq. 2.8 was derived by assigning the value of 2 to λ and using the following model to represent relative permeability:

$$k_{rw} = (S_w^*)^4 \tag{2.9}$$

According to Eq. 2.8, the wettability index is also proportional to the normalized wetting phase saturation if the Corey model (1954) is used to represent the relationship between relative permeability and capillary pressure.

The rock property factors, including the pore size distribution index λ, the permeability k, the porosity ϕ, and the lithology factor F, may be omitted when Eq. 2.1 is used to compare the wettability differences between two different fluid pairs such as gas-water and oil-water (in the same rock). The ratio of the wettability index of fluid pair 1 to fluid pair 2 at the same water saturation and in the same rock can be obtained from Eq. 2.1:

$$\frac{W_{iw}^1}{W_{iw}^2} = \frac{k_{rw}^1}{k_{rw}^2}\frac{P_c^1}{P_c^2}\frac{\sigma^2}{\sigma^1} \tag{2.10}$$

where W_{iw}^n, k_{rw}^n, P_c^n, and σ^n (n=1, 2) are the wettability index, the relative permeability of the wetting phase, the capillary pressure, and the interfacial tension in fluid pair n (=1, 2) respectively. It is only necessary to obtain the capillary pressure and the relative permeability data in order to compare the wettability in two different fluid systems.

If the relative permeabilities of the wetting phase in the two fluid pairs are equal, Eq. 2.10 could be reduced to the form of the Slobod and Blum model (1952), which is:

$$W_r = \frac{W_{iw}^1}{W_{iw}^2} = \frac{P_c^1}{P_c^2}\frac{\sigma^2}{\sigma^1} \tag{2.11}$$

where W_r is the ratio of the wettability index of fluid pair 1 to fluid pair 2. As stated previously, it was assumed that the contact angle through the liquid phase in the gas-liquid-rock system was zero in the Slobod and Blum model (1952). Hence W_{iw}^2 (representing wettability index of the gas-liquid fluid pair) is equal to one in this case. Note that the relative permeabilities of the wetting phase measured using two different fluid pairs may not be always equal.

2.4 RESULTS

The experimental data of nitrogen-water relative permeability and capillary pressure in Berea sandstone from Li and Horne (2001b) were used to calculate the wettability index of nitrogen-water-rock systems. The Berea core sample we used in Li and Horne (2001b) was fired at high temperature to remove the clay. The permeability and porosity of the rock were 1280 md and 23.4%; the length and diameter were 43.2 cm and 5.08 cm respectively. Both the relative permeability and capillary pressure data published in Li and Horne (2001b) are depicted in Fig. 2.1.

According to Eq. 2.1, it is necessary to obtain the value of the lithology factor F to calculate the wettability index. To this end, mercury injection was conducted after the measurement of nitrogen-water capillary pressure in a plug drilled from the long core. The capillary pressure curve measured by the mercury injection technique is shown in Fig. 2.2.

Using the capillary pressure data in Fig. 2.2 and the measured absolute permeability (1200 md) of the plug, the value of *F* was calculated and was equal to 0.129.

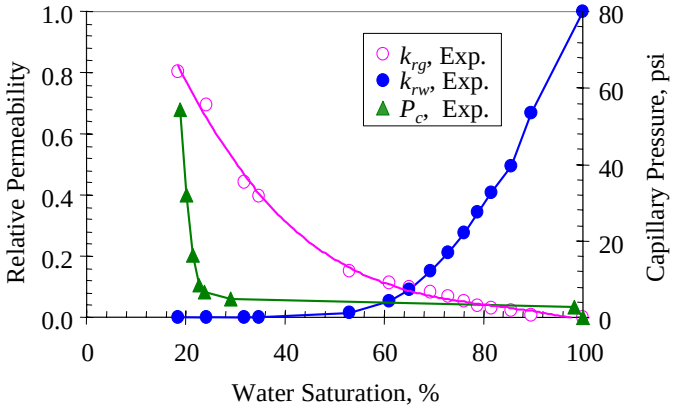

Figure 2-1: Experimental data of drainage nitrogen-water relative permeability and capillary pressure.

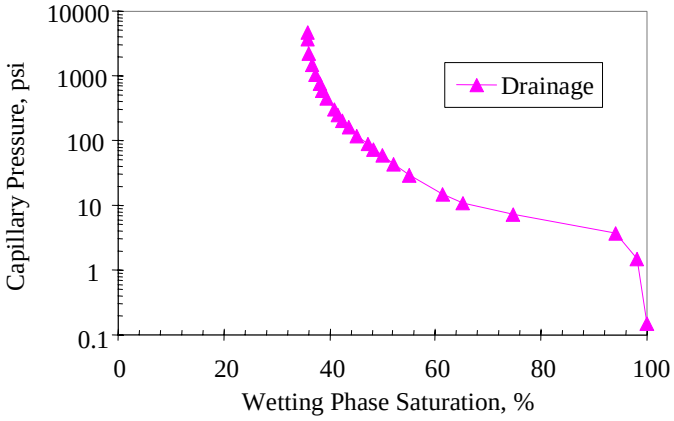

(a): Capillary pressure curve.

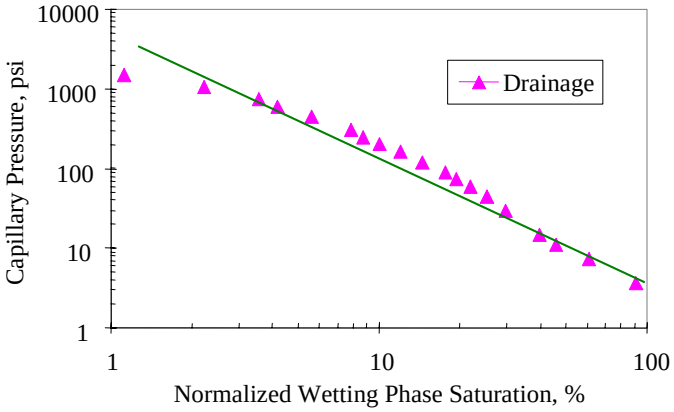

(b): Fit using the Brooks-Corey model.

Figure 2.2: Capillary pressure of fired Berea measured by mercury injection.

Purcell (1949) measured the values of F in many reservoir rock samples. The F data from Purcell (1949) and this study are plotted in Fig. 2.3, as a function of air permeability. Also shown in Fig. 2.3 is the value of F of the Berea sandstone before it was fired. It can be seen from Fig. 2.3 that the relationship between the lithology factor and the air permeability is closely linear on a log-log plot for all the data, including the F values in Berea sandstone. The mathematical expression for such a relationship obtained by regression is represented as follows:

$$F = 0.0465 k_{air}^{0.1519} \tag{2.12}$$

Eq. 2.12 can be used to estimate the value of F according to the air permeability of rock when mercury injection capillary pressure is not available. Note that there is a factor of 2 difference between the lithology factor defined in this study and that defined by Purcell (1949).

The value of the pore size distribution index can be calculated by fitting the nitrogen-water capillary pressure data shown in Fig. 2.1 using Eq. 2.3. The calculated value of λ for the core sample was 1.15.

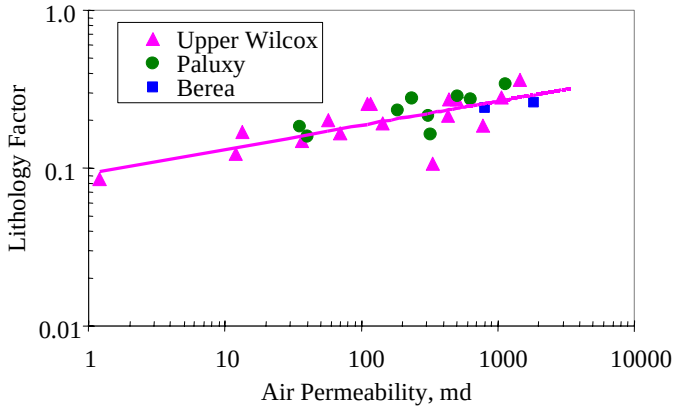

Figure 2.3: Relationship between lithology factor and air permeability in reservoir rock and Berea sandstone.

The values of wettability index were calculated using Eqs. 2.1, 2.5, 2.7, and 2.8 with the experimental and model data of relative permeability and capillary pressure. The results are shown in Fig. 2.4. The wettability index calculated using the Purcell model data (the required relative permeabilities were obtained by fitting the experimental data using Eq. 2.2) does not change with water saturation. However the wettability index increases linearly with the normalized water saturation when relative permeability and capillary pressure are represented using the Corey model (1954) or the Brooks-Corey model (B-C model in Fig. 2.4). This behavior is similar to that of the wettability index calculated using the experimental data of relative permeability and capillary pressure. Note that Li and Horne (2002) showed that the wettability index calculated using the experimental data of relative permeability and capillary pressure did not change with water saturation in some

oil-water-rock systems. An important feature shown in Fig. 2.4 is that the values of the wettability index calculated using different equations (Eqs. 2.1, 2.5, 2.7, and 2.8) are closer to each other at higher normalized water saturation.

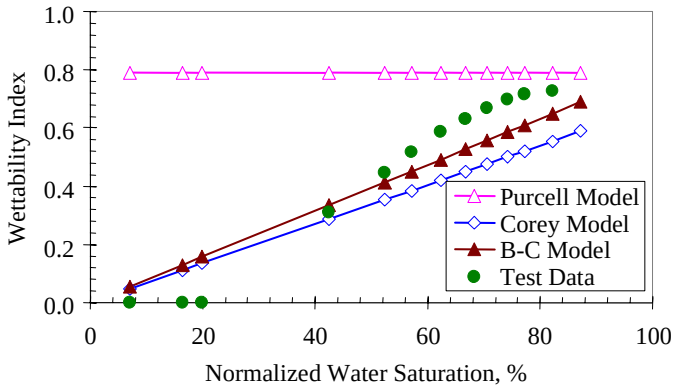

Figure 2.4: Wettability indices calculated using capillary pressure and relative permeability of nitrogen-water-rock (Berea) systems.

It is often assumed that wettability does not change with water saturation. This may be true in some cases, as we showed in Li and Horne (2002). This may not be true in other cases, as demonstrated in Fig. 2.4. More investigation on the relationship between wettability and water saturation is required.

We made the same calculation using the data of oil-gas relative permeability and capillary pressure measured in Berea sandstone by Richardson *et al*. (1952). The permeability and porosity of this core were 107 md and 17.7%; the length and diameter were 30.7 cm and 6.85 cm, respectively. The oil phase was kerosene and the gas phase was helium. The experimental data of the drainage oil-gas relative permeability and the capillary pressure are shown in Fig. 2.5. The value of F for this core sample was calculated using Eq. 2.12. Fig. 2.6 shows the values of the wettability index of the gas-oil-rock system at different wetting phase saturations using different methods (Eqs. 2.1, 2.5, 2.7, and 2.8). The wettability index calculated using the Purcell model data does not change with the wetting phase saturation while those calculated using the Corey model or the Brooks-Corey model data increase linearly with the normalized wetting phase saturation. In this case, the wettability indices calculated using Eq. 2.5 with the Purcell model data of relative permeability and the capillary pressure have a better representation of those calculated using the experimental data of relative permeability and the capillary pressure.

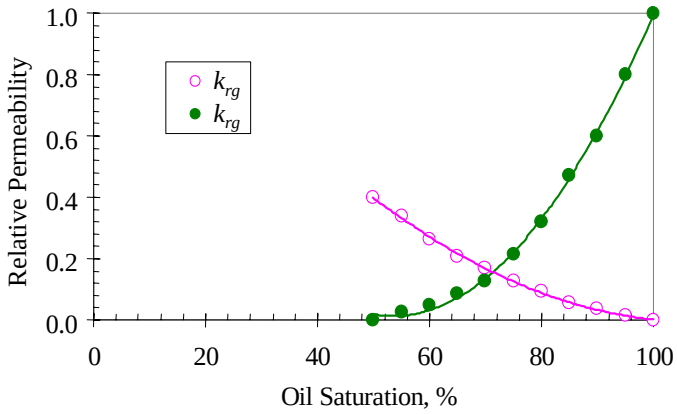

(a) Relative permeability curve

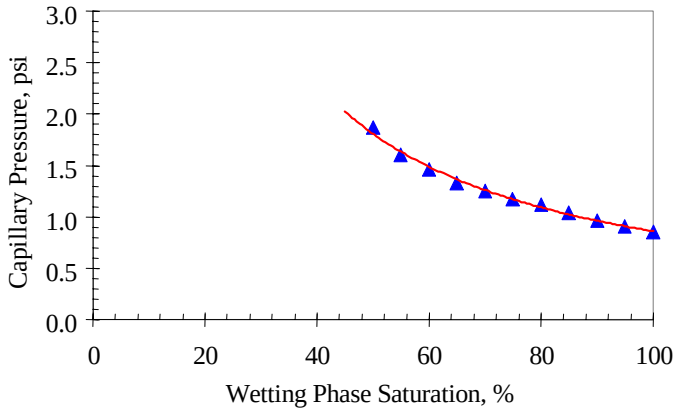

(b) Capillary pressure curve

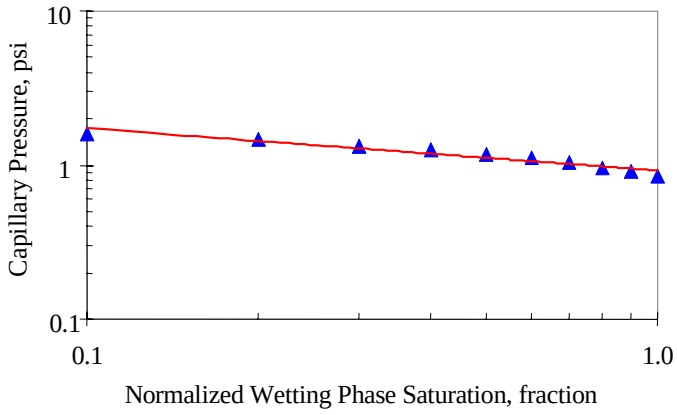

(c) Fit using the Brooks-Corey model

Figure 5: Experimental data of drainage gas-oil relative permeability and capillary pressure (Richardson et al., 1952).

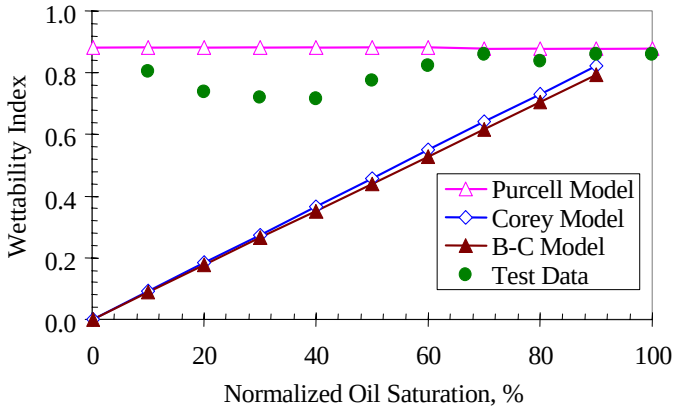

Figure 6: Wettability indices calculated using capillary pressure and relative permeability of gas-oil-rock (Berea) systems.

It is important to verify the validity of the method (representing by Eq. 2.1) to evaluate wettability of gas-liquid-rock and liquid-liquid-rock systems.

Fig. 2.7 shows the values of the wettability index in both drainage and imbibition cases. The wettability indices were calculated using Eq. 2.5 with the experimental data in steam-water-rock systems (Li and Horne, 2001c and 2001d). The value of *F* for the core sample was the same as that calculated using the mercury injection capillary pressure data shown in Fig. 2.2. This is because the core sample used to measure the steam-water relative permeability and capillary pressure was almost the same as that used to measure the nitrogen-water relative permeability. One can see from Fig. 2.7 that the wettability index calculated using Eq. 2.5 is greater in drainage than that in imbibition, as is already known. This observation confirms the validity of the method. The value of *F* was not available in our previous results (Li and Horne, 2002) because the measurement of capillary pressure by mercury injection was not available at the time.

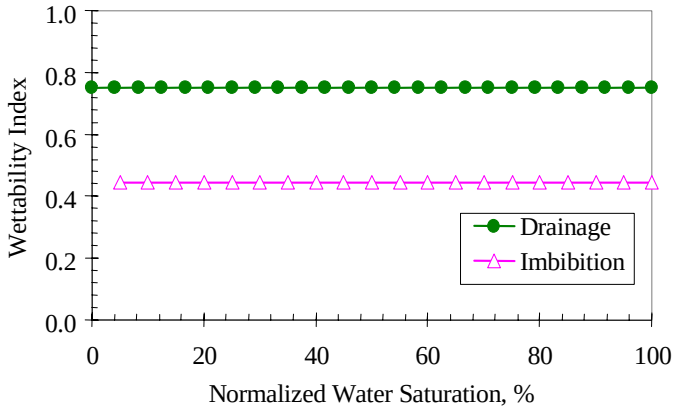

Figure 7: Wettability indices calculated in drainage and imbibition in steam-water-rock (Berea) systems.

It is also known that the wettability index in gas-liquid-rock systems is greater than that in liquid-liquid-rock systems. This may also be used to test the validity of the method represented by Eq. 2.1. Fig. 2.8 shows the values of the wettability index in drainage in a gas-oil-rock (Berea) system and those in imbibition in a water-oil-rock (Berea) system. The data in drainage in a water-oil-rock (Berea) system is not available. All the values of the wettability index were calculated using the Purcell model data of relative permeability and capillary pressure. One can see from Fig. 2.8 that the wettability for the wetting phase in a gas-oil-rock (Berea) system is much stronger than that in a water-oil-rock (Berea) system, which is reasonable and consistent with the present understanding.

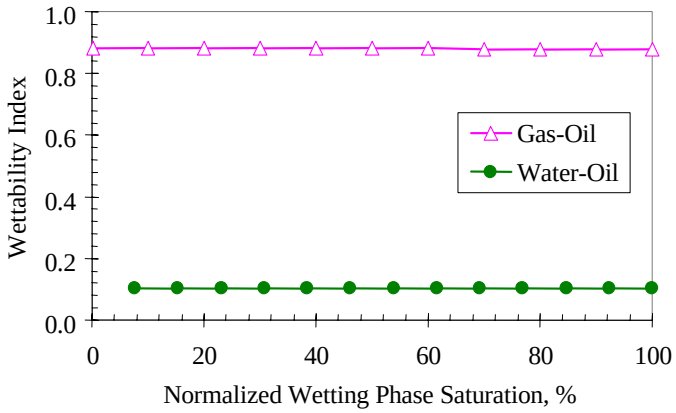

Figure 8: Wettability indices of gas-oil-rock and water-oil-rock (Berea) systems.

The preceding verification to the validity of the method represented by Eq. 2.1 is only qualitative. It would be useful to verify the validity quantitatively. To do so, the experimental data from Morrow (1976) were used. According to Eq. 2.5, only capillary pressure data are required to determine the wettability index. The capillary pressure curves measured in different gas-liquid-rock systems with different known contact angles (or wettability index) are depicted in Fig. 2.9.

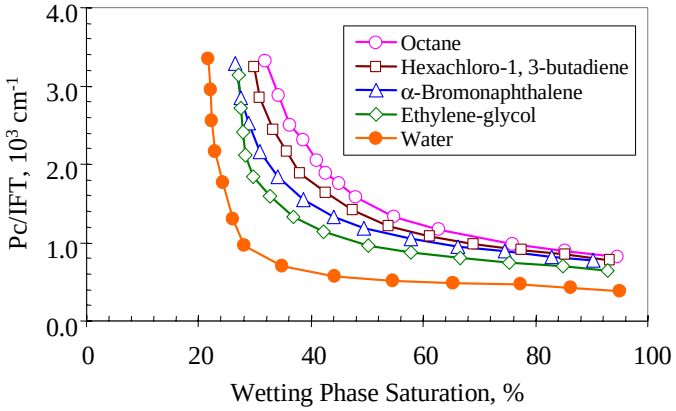

Figure 2.9: Experimental data of drainage capillary pressure curves in gas-liquid-PTFE systems (Morrow, 1976).

It is necessary to fit the experimental data of capillary pressure using Eq. 2.3 in order to obtain the values of the pore size distribution index. The wetting phase saturation data were normalized using Eq. 2.4 and the relationships between capillary pressure and the normalized wetting phase saturation are shown in Fig. 2.10. Most of the relationships are linear on a log-log plot.

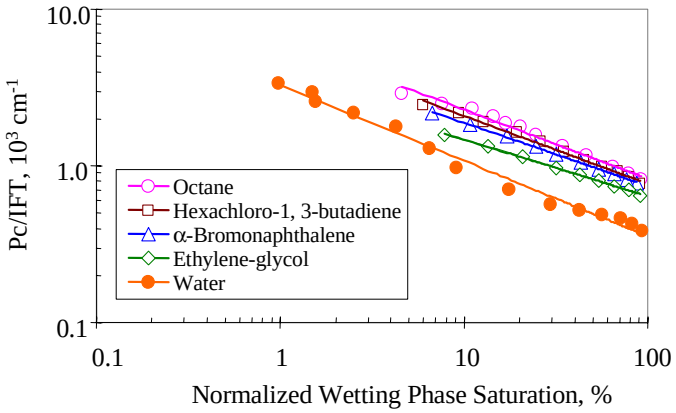

Figure 2.10: Fit the drainage capillary pressure curves in gas-liquid-PTFE systems using the Brooks-Corey model.

The values of λ were calculated using the relationships shown in Fig. 2.10 and were used to calculate the wettability index in drainage. The results calculated using Eq. 2.5 are compared to the values of the wettability measured by Morrow (1976), as shown in Fig. 2.11. One can see that the values of the wettability index calculated using Eq. 2.5 are close to the experimental data of the wettability index except one point. However the number of data points is limited. Note that the wettability index in the gas-Octane-PTFE system was assumed to be 1 to obtain the value of *F* of the core sample.

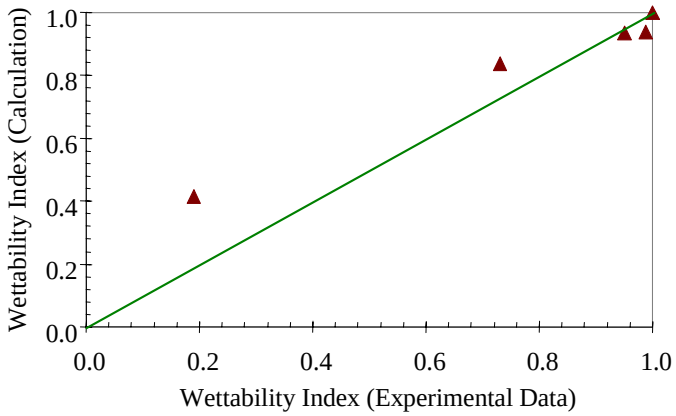

Figure 2.11: Comparison of wettability indices calculated using the proposed method to the measured values.

2.5 CONCLUSIONS

Based on the present study, the following conclusions may be drawn:

1. The proposed method can be used to determine the wettability of both gas-liquid-rock systems and liquid-liquid-rock systems.
2. The wettability index at any specific water saturation may be determined using the method. It has been found that the wettability index may or may not change with fluid saturation in the cases studied.
3. The values of the wettability index calculated using the proposed technique are much greater in gas-liquid-rock systems than those in liquid-water-rock systems. The values in imbibition are smaller than in drainage as expected. This demonstrates the qualitative validity of the proposed method.
4. The results showed that the often-used assumption, that the contact angle through the liquid phase is zero in gas-liquid systems, may be true in some cases but may not be true in other cases.

3. REFERENCES

Brooks, R. H. and Corey, A. T.: "Properties of Porous Media Affecting Fluid Flow", *J. Irrig. Drain. Div*., (1966), 6, 61.

Chen, C.-Y., Diomampo, G., Li, K. and Horne, R.N.: "Steam-Water Relative Permeability in Fractures," *submitted to Geothermal Resources Council Transactions Vol.26*, 2002.

Corey, A. T.: "The Interrelation between Gas and Oil Relative Permeabilities", *Prod. Mon*., (1954), **19**, 38.

Diomampo, G., "Relative Permeability through Fracture", MS thesis, Stanford University, Stanford, California (2001).

Diomampo, G., Chen, C.-Y, Li, K. and Horne, R.N.: "Relative Permeability through Fractures," *Proc. 27th Workshop on Geothermal Reservoir Engineering*, Stanford University, Stanford, California, January 28-30, 2002.

Fourar, M. and Bories, S.,: "Experimental Study of Air-Water Two-Phase Flow Through A Fracture (Narrow Channel)," *Int. J. Multiphase Flow* Vol. 21, No. 4, (1995) pp. 621-637.

Fourar, M., Bories., Lenormand, R., and Persoff, P.,: "Two-Phase Flow in Smooth and Rough Fractures: Measurement and Correlation by Porous-Medium and Pipe Flow Models," *Water Resources Research* Vol. 29 No. 11. November 1993, pp. 3699-3708.

Horne, R.H., Satik, C., Mahiya, G., Li, K., Ambusso, W., Tovar, R., Wang, C., and Nassori, H.: "Steam-Water Relative Permeability," *Proc. of the World Geothermal Congress* 2000, Kyushu-Tohoku, Japan, May 28-June 10, 2000.

Kneafsy, T. J. and Pruess, K.,: "Laboratory Experiments on Heat-Driven Two-Phase Flows in Natural and Artificial Rock Fractures," *Water Resources Research* Vol. 34, No. 12, December 1998, pp. 3349-3367.

Li, K., and Horne, R.N., "Accurate Measurement of Steam Flow Properties," *GRC Transactions* 23 (1999).

Li, K. and Horne, R.N. (2001a): "Characterization of Spontaneous Water Imbibition into Gas-Saturated Rocks," *SPEJ* (December 2001), **6**(4), p.375-384.

Li, K. and Horne, R.N. (2001b): "Gas Slippage in Two-Phase Flow and the Effect of Temperature," SPE 68778, presented at the 2001 SPE Western Region Meeting, Bakersfield, CA, USA, March 26-30, 2001.

Li, K. and Horne, R.N. (2001c): "An Experimental and Theoretical Study of Steam-Water Capillary Pressure," *SPEREE* (December 2001), p.477-482.

Li, K. and Horne, R.N. (2001d): "Steam-Water Relative Permeability by the Capillary Pressure Method," proceedings of the International Symposium of the Society of Core Analysts, Edinburgh, UK, September 17-19, 2001.

Li, K. and Horne, R.N.: "Wettability of Steam-Water-Rock Systems," presented at the 7th International Symposium on Reservoir Wettability, Freycinet, Tasmania, Australia, March 12-15, 2002.

Lockhart, R. W. and Martinelli, R.C.,: "Proposed Correction of Data for Isothermal Two-Phase Component Flow in Pipes," *Chem. Eng. Prog*., Vol. 45, No. 39, 1949.

Mahiya, G., "Experimental Measurement of Steam-Water Relative Permeability," MS thesis, Stanford University, Stanford, California (1999).

Morrow, N.R.: "Capillary Pressure Correlations for Uniformly Wetted Porous Media," *JCPT* (October, 1976), 49-69.

Pan, X., Wong, R.C., and Maini, B.B.: Steady State Two-Phase Flow in a Smooth Parallel Fracture, presented at the 47th Annual Technical Meeting of the Petroleum Society in Calgary, Alberta, Canada, June 10-12, 1996.

Persoff, P. K., Pruess, K., and Myer, L.: "Two-Phase Flow Visualization and Relative Permeability Measurement in Transparent Replicas of Rough-Walled Rock Fractures," *Proc. 16th Workshop on Geothermal Reservoir Engineering*, Stanford University, Stanford, California, January 23-25, 1991

Persoff, P., and Pruess, K.: "Two-Phase Flow Visualization and Relative Permeability Measurement in Natural Rough-Walled Rock Fractures," *Water Resources Research* Vol. 31, No. 5, May, 1995, pp. 1175-1186.

Pruess, K., and Tsang, Y. W.: "On Two-Phase Relative Permeability and Capillary Pressure of Rough-Walled Rock Fractures," *Water Resources Research* Vol. 26 No. 9, September 1990, pp 1915-1926.

Purcell, W.R.: "Capillary Pressures-Their Measurement Using Mercury and the Calculation of Permeability", *Trans. AIME*, (1949), 186, 39.

Richardson, J.G., Kerver, J.K., Hafford, J.A., and Osoba, J.S.: "Laboratory Determination of Relative Permeability", *Trans. AIME*, (1952), **195**, 187.

Scheidegger, A.E. *The Physics of Flow Through Porous Media*, 3rd ed., University of Toronto, Toronto. 1974.

Slobod, R.L. and Blum, H.A.: "Method for Determining Wettability of Reservoir Rocks", *Trans. AIME*, (1952), 195, 1.

Su, G. W., Geller, J. T., Pruess, K. and Wen, F.,: " Experimental Studies of Water Seepage and Intermittent Flow in Unsaturated, Rough-Walled Fractures," *Water Resources Research*, Vol. 35, No. 4, April 1999, pp. 1019-1037.

Witherspoon, P.A., Wang, J.S.W., Iwai, K. and Gale, J.E.: " Validity of Cubic Law for Fluid Flow in a Deformable Rock Fracture," *Water Resources Research*, Vol. 16, No. 6, 1980, pp 1016-1024.